

**TIDALLY-FORCED
VORTICITY, DIURNAL SHEAR AND TURBULENCE
ATOP FIEBERLING SEAMOUNT**

by

Eric Kunze*
John M. Toole†

*Oceanography, U of Washington
Box 357940
Seattle, WA 98195-7940

†Woods Hole Oceanographic Institution
Woods Hole, MA 02543

19960429 047

DISTRIBUTION STATEMENT A

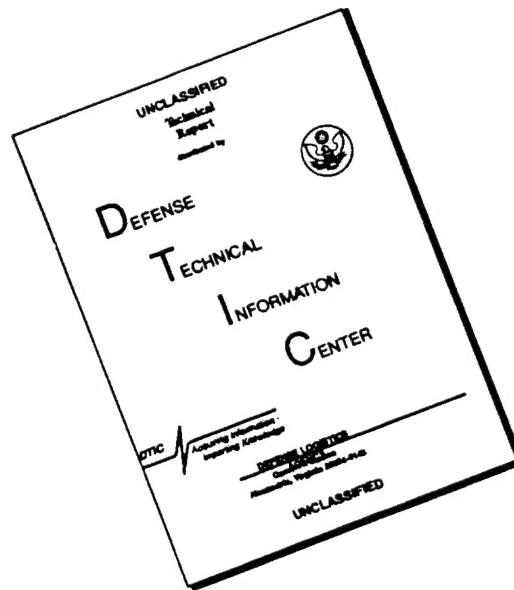
Approved for public release:
Distribution Unlimited

MAR 1996

submitted to *J. Phys. Oceanogr.*

DTIC QUALITY INSPECTED 1

DISCLAIMER NOTICE



THIS DOCUMENT IS BEST QUALITY AVAILABLE. THE COPY FURNISHED TO DTIC CONTAINED A SIGNIFICANT NUMBER OF PAGES WHICH DO NOT REPRODUCE LEGIBLY.

ABSTRACT

Fine- and microstructure profiles collected over Fieberling Seamount at $32^{\circ}26'N$ in the eastern North Pacific reveal three intensified phenomena co-existing in a 200-m thick layer atop the summit plain: (i) an anticyclonic vortex cap of core relative vorticity $-0.50f$, (ii) diurnal shear of $15 \text{ cm s}^{-1}/40 \text{ m}$, and (iii) turbulence levels corresponding to an eddy diffusivity $K_p \approx 10 \times 10^{-4} \text{ m}^2 \text{ s}^{-1}$. The vortex cannot be explained solely by Taylor-Proudman dynamics because of its $-0.3fN^2$ negative potential vorticity anomaly. The fortnightly cycle in the vortex's strength suggests that it is at least partially maintained against dissipative erosion by rectification of diurnal tides. Baroclinic diurnal fluctuations are slightly subinertial and the diurnal kinetic energy also tracks the beating of the barotropic K_1 and O_1 diurnal tides. Their horizontal structure closely resembles a seamount-trapped topographic wave. However, counterclockwise turning with depth of the horizontal velocity vector and the 180° phase difference between radial velocity u_r' and vertical displacement $\xi' = -T'/\bar{T}_z$ (producing a net positive radial heat-flux $\langle u_r'T' \rangle$) are more consistent with an upward-propagating vortex-trapped near-inertial internal wave. The slightly subinertial frequency is allowed by the strong negative vorticity of the vortex cap. A vortex-trapped wave would encounter a vertical critical layer at the top of the cap where its energy would be lost to turbulence. High observed turbulence levels of $\varepsilon = 3 \times 10^{-8} \text{ W kg}^{-1}$ imply decay times for the wave and vortex of less than 3 days, emphasizing the strongly forced nature of the system. Inferred eddy diffusivities two orders of magnitude larger than those found in the ocean interior suggest that, locally, seamounts are important sites for diapycnal transport. On basin scales, however, there are too few seamounts penetrating the main pycnocline to produce a basin-averaged diffusivity of $O(10^{-4} \text{ m}^2 \text{ s}^{-1})$. Interior and near-bottom mixing likely contribute comparable diapycnal buoyancy-fluxes at these depths.

1. INTRODUCTION

The peaks of seamounts have been found to be sites of enhanced near-bottom subinertial, diurnal, inertial and semidiurnal currents (Noble *et al.* 1988; Noble and Mullineaux 1989; Genin *et al.* 1989; Padman *et al.* 1992; Eriksen 1991; Kunze and Sanford 1986; Kunze *et al.* 1992). These elevated velocities support abundant populations of benthic filterfeeders (Genin *et al.* 1986; 1992; Levin *et al.* 1994). How topography intensifies these currents is not established. Kunze and Sanford (1986) interpreted their signal as a critically-reflected upward-propagating near-inertial wave based on the counterclockwise turning of its horizontal velocity with depth. On the other hand, Genin *et al.* (1989), Eriksen (1991; 1995b), Noble *et al.* (1994) and Brink (1995a) report slightly subinertial diurnal tidal frequencies associated with the dominant motions above Fieberling Guyot so they advanced that the fluctuations might be seamount-trapped topographic waves (Brink 1989; 1990).

Sloping topography allows bottom-trapped topographic waves with frequencies $\omega \leq N \sin \alpha$ (Rhines 1970; Huthnance 1978). Sloping bottom topography will also cause internal waves with characteristic slopes $C_{gz}/C_{gH} = k_H/k_z$ identical to the bottom slope α to be critically reflected (Wunsch 1969; Phillips 1977; Eriksen 1982; 1985) and scattered to high wavenumbers (Baines 1971; Bell 1975; Gilbert and Garrett 1989; Müller and Xu 1992), dramatically amplifying internal-wave shear and strain. Enhanced finescale shear and strain will support stronger and more frequent shear/advection instability to produce intensified turbulence (Henyey *et al.* 1986; Gregg 1989; Polzin *et al.* 1995). Relative to the ocean interior, enhanced turbulence has been documented over seamounts (Nabatov and Ozmidov 1988; Lueck and Mudge 1996; Toole *et al.* 1996). This has led to speculation that seamounts act as stirring rods for the world ocean, with topographically-induced mixing near boundaries dominating over the weak diapycnal mixing of the ocean interior (Lueck and Mudge 1996).

Mean circulations are also expected over seamounts. Both Taylor-Proudman dynamics (Hogg 1973; Swaters and Mysak 1985; Roden 1987) and topographic rectification processes (Loder 1980; Maas and Zimmerman

1989a; 1989b; Haidvogel *et al.* 1993) could lead to formation of a vortex cap over a seamount's summit. Stratification limits the vertical extent of vortices above seamounts (Zyryanov 1981; Chapman and Haidvogel 1992) to $H = fL/N$. For Coriolis frequency $f = 7.8 \times 10^{-5} \text{ s}^{-1}$, buoyancy frequency $N = 4.3 \times 10^{-3} \text{ s}^{-1}$ and seamount radius $L = 7 \text{ km}$, the cap thickness $H \sim 100 \text{ m}$. A Taylor cap would be anticyclonic and requires an impinging geostrophic flow. In the absence of damping, this vortex would have the same potential vorticity as the surrounding ocean. The properties of a rectification-driven vortex depend on the nature of the forcing and damping and are less certain. They need neither be anticyclonic nor preserve potential vorticity.

To better understand the impact of seamounts on internal waves, tides and turbulent mixing, fine- and microstructure profiles were collected over Fieberling Guyot during March 1991 (Montgomery and Toole 1993). Here we use the profile time-series and surveys to characterize the temporal and spatial structure of motions atop Fieberling Guyot's summit plain. Toole *et al.* (1996) examine the turbulent boundary layer above the seamount's flanks. We find a vortex cap atop Fieberling Guyot that is $\sim 200\text{-m}$ thick, has a core vorticity $\zeta = -(0.50 \pm 0.15)f$ and a core potential vorticity anomaly of $-0.3fN^2$. The presence of this anticyclonic vortex raises the possibility that the diurnal oscillations coinciding with the vortex are not seamount-trapped topographic waves but vortex-trapped near-inertial internal waves (Kunze *et al.* 1995). Maximum velocities of the diurnal motion over Fieberling Guyot's summit plain are $\sim 15 \text{ cm s}^{-1}$ some 50-100 m above the bottom over the summit plain. This signal decays rapidly with radial distance away the seamount. At any instant and depth, the horizontal velocity of the diurnal motion forms a unidirectional jet over the summit which turns clockwise in time. This horizontal structure is consistent with either the gravest seamount-trapped mode (Brink 1990) or the gravest vortex-trapped internal wave mode (Kunze *et al.* 1995). The velocity vector also turns counterclockwise with depth over the entire 200-m thick layer of intensified motion with a vertical turning wavelength $\lambda_z = 250 \text{ m}$. If interpreted as a vortex-trapped near-inertial wave, it implies upward energy propagation. It contradicts (i) Brink's (1990) predicted turning of only $\sim 90^\circ$ confined to within 50 m of the bottom due to bottom friction and a weak

counterclockwise-propagating component, and (ii) the turning wavelength for a time-dependent nonlinear benthic Ekman layer (e.g., Brink 1995b). Beckmann and Haidvogel's (1996) numerical simulation of Fieberling reproduces most of the above observed features though their simulated vortex is 400- rather than 200-m thick.

Elevated turbulence dissipation rates $\epsilon \approx 10^{-7} \text{ W kg}^{-1}$ coincide with the vortex cap and the diurnal oscillation, sufficient to drain the wave and vortex in less than three days if they are the energy sources for the turbulence. This highlights the strongly forced nature of motions atop the seamount's summit plain; without the barotropic tide continually pumping energy into the system, it would rapidly run down. The corresponding eddy diffusivities are of order $10 \times 10^{-4} \text{ m}^2 \text{ s}^{-1}$. These are two orders of magnitude larger than those deduced for the surrounding ocean, suggesting that, locally at least, seamounts are important sites for diapycnal exchange.

2. TRAPPED WAVE MODELS

In a stratified fluid, the barotropic diurnal tide impinging on a seamount will generate baroclinic oscillations in order to satisfy the no-normal-flow boundary condition. Three extant models may describe the intensified baroclinic diurnal motions observed above the summit plain of Fieberling Guyot — near-resonant seamount-trapped topographic waves (Brink 1989), forced (off-resonant) evanescent topographic fluctuations (Brink 1990; Eriksen 1995b) and vortex-trapped near-inertial internal waves (Kunze *et al.* 1995). We will refer to slightly off-resonant forced oscillations as waves here even though they do not exactly satisfy the dispersion relation or consistency relations for free waves. These three types of waves share many properties in common and their observable differences are subtle. We caution that all of these models are approximate. The topographic wave models neglect background mean shear and the vortex-trapped model treats shear crudely.

2.1 Seamount-trapped topographic waves

Brink (1989) formulated a model for free seamount-trapped waves on tall seamounts in a stratified, rotating fluid, extending the barotropic models of Rhines (1969), Huthnance (1974), Hunkins (1986) and Chapman (1989). These waves are bottom-trapped topographic waves (Rhines 1970) wrapped around a seamount so that their along-isobath wavenumber is quantized.

For the stratification profile and geometry of Fieberling Guyot, Brink (1990) showed that the gravest (highest frequency) seamount-trapped mode had a slightly subinertial frequency (29-h period) and was nearly resonant with the diurnal tide. This mode evanesces rapidly away from the bottom with a vertical decay scale of ~ 50 m and a radial decay scale of a few kilometers (radial mode 0). The first azimuthal mode is most likely to be excited by largescale forcing because its flow direction is the same on all sides of the seamount (Brink 1990). The direction of the resulting jet rotates clockwise in time and propagates clockwise around the seamount.

2.2 Forced evanescent waves

Brink (1990) extended his free-wave work to investigate the free-mode expansion of the on- and off-resonance forced response. Laboratory experiments (Codiga 1993; Boyer and Zhang 1990; Zhang and Boyer 1993) and numerical simulations (Haidvogel *et al.* 1993; Beckmann and Haidvogel 1996) have verified generation of baroclinic subinertial seamount-trapped oscillations by barotropic forcing in stratified, rotating fluids. Forced, topographically-trapped motions can be off-resonant and thus do not satisfy zero normal flow at the bottom; this is necessary for them to compensate the normal flow of the forcing. However, if they are only slightly off resonance, evanescent fluctuations closely resemble free topographic waves. For example, eddy viscous/diffusive damping alters the phase consistency relations for seamount-trapped waves by only a few degrees for the wavelengths of interest (Appendix B). Observationally, Brink's off-resonance predictions are consistent with the diurnal frequency and horizontal structure of the dominant velocity fluctuations above the summit plain of Fieberling Seamount (Eriksen 1991; Noble *et al.* 1994; Brink 1995a).

One of the few ways for distinguishing between gravest free or forced seamount-trapped oscillations and vortex-trapped waves (section 2.3) is with the phase relation between radial velocity u_r' and vertical displacement ξ' signals. For (i) the cross-slope standing modes discussed by Brink, (ii) topographic waves propagating across the slope, and (iii) a slightly off-resonance forced bottom-trapped response, u_r' is roughly out of phase with ξ' and v_θ' . This implies that inviscid seamount-trapped oscillations have near-zero radial heat-flux, $\langle u_r' T' \rangle \approx 0$, and finite azimuthal heat-flux, $\langle v_\theta' T' \rangle$.

The horizontal velocity vector for cross-slope standing seamount-trapped modes undergoes 180° reversals, but no turning with depth. A benthic Ekman layer will induce counterclockwise-turning-with-depth near the bottom and a velocity maximum above the bottom. Brink (1995b) developed a model for time-dependent Ekman layers in the presence of relative vorticity. His expression for the real part of the wavenumber (the

part associated with phase propagation and turning of the velocity vector with depth) is

$$k_{z\pm} = \pm \frac{\sqrt[4]{\zeta^4 w_0^4 + 16f^2(\omega_i \pm f_{eff})^2 \sin(\theta/2)}}{2\sqrt{f}V_e} \quad (1)$$

where $\theta = \text{Arctan}[(4f(\omega_i \pm f_{eff})/(\zeta^2 w_0^2))]$, $w_0 \sim O(1)$ is the nondimensional vertical velocity at the top of the Ekman layer associated with the Ekman downwelling that arises in this geometry, $\omega_i = \omega_E - nV_\theta/r \simeq \omega_E - n\zeta/2 = K_1 + \zeta/2$ the intrinsic frequency, $f_{eff} = f + \zeta$ the effective Coriolis frequency, ω_E the Eulerian frequency, V_θ the azimuthal velocity of the vortex and $\zeta = V_\theta/r + \partial V_\theta/\partial r$ its relative vorticity. Except near the zero of $\omega - f_{eff}$, the wavenumber can be approximated as

$$k_{z\pm} = \sqrt{\frac{\omega \pm f_{eff}}{V_e}}.$$

Relation (1) will be compared with the observations in Fig. 14.

2.3 Vortex-trapped near-inertial internal waves

Anticyclonic vorticity reduces the lower bound of the internal waveband from the planetary Coriolis frequency f to an effective Coriolis frequency f_{eff} (Weller 1982; Kunze 1985). As shown by Kunze *et al.* (1995), for a vortex in solid-body rotation and a wave treated in cylindrical coordinates, the effective Coriolis frequency $f_{eff} = f + \zeta$ ($= 0.5f$ for a vorticity of $-0.5f$ as characterizes the core above Fieberling, Fig. 3); half the modulation arises from interaction with the background shear $\partial V_\theta/\partial r$, and half from advection (Doppler-shifting) by the background flow V_θ/r (Appendix B of Kunze 1985). The effective Coriolis frequency is well below the diurnal frequencies $K_1 = 0.933f = 1.87f_{eff}$ and $O_1 = 0.865f = 1.73f_{eff}$, permitting diurnal frequencies to propagate as near-inertial internal waves within the confines of the negative vorticity core. Like the seamount-trapped wave, such an oscillation would arise above Fieberling to satisfy the no-

normal-flow bottom boundary condition (e.g., Baines 1982). Kunze *et al.* (1995) formulated a model for a vortex-trapped, near-inertial radial mode while investigating near-inertial wave critical layers in a warm-core ring. In this model, the superposition of plane waves reflecting off the lateral walls of the vortex sets up a radial mode which closely resembles a seamount-trapped wave in its horizontal structure. Like the seamount-trapped wave, the most likely azimuthal mode that will be excited by largescale clockwise rotary forcing is $n = -1$, corresponding to clockwise azimuthal propagation around the vortex. The intrinsic, or Lagrangian, frequency is then $\omega_i = \omega_E - nV_\theta/r \approx K_1 + \zeta/2 = 0.933f - 0.25f = 0.683f > f_{eff}$. Like the gravest seamount-trapped wave, this mode has maximum horizontal velocity amplitude near vortex center and, at any given instant, forms a nearly unidirectional jet in the vortex core. Decay is rapid moving radially out of the vortex. The orientation of the jet rotates clockwise in time.

Unlike the seamount-trapped topographic wave, a vortex-trapped wave is an internal wave and is therefore free to carry energy and momentum upward into the overlying water column. For a near-inertial wave of upward energy propagation, the horizontal velocity vector turns counterclockwise with depth. With frequency $\omega_i = \omega_E + \zeta/2$ set by the forcing, and lateral scales λ_r dictated by the vortex dimensions, the vertical wavelength is given by the dispersion relation

$$\lambda_z = \lambda_r \frac{\sqrt{\omega_i^2 - f_{eff}^2}}{N} \quad (2)$$

where λ_r is the radial wavelength (Kunze *et al.* 1995). Relation (2) will be compared to the observations in Fig. 18. Since internal waves can propagate freely only where $\omega_i > f_{eff}$, that is, inside the vortex, they reflect off horizontal turning points on the vortex sides to set up radial modes. Upward propagation is blocked at a vertical critical layer at the top of the vortex where energy will accumulate until instabilities transfer it to dissipative turbulence (Kunze *et al.* 1995). Thus, for a vortex-trapped wave, maxima in energy, shear and turbulent dissipation are expected above the bottom.

For upward and clockwise azimuthal propagation, the radial velocity u_r' is 180° out of phase with the vertical displacement $\xi' = -T'/\bar{T}_z$, giving a net outward radial heat-flux $\langle u_r' T' \rangle$. In the absence of irreversible processes (forcing and dissipation), this wave flux will be balanced by a wave-induced mean advective radial heat-flux. Including eddy diffusivities and viscosities ranging up to $10 \times 10^{-4} \text{ m}^2 \text{ s}^{-1}$, consistent with the microstructure measurements, does not significantly alter the dispersion relation between frequency, vertical wavenumber and horizontal wavenumber (2), nor the consistency relations between horizontal velocity components, u_r' and v_θ' . Thus, it will not alter the turning of the velocity vector with depth. The phase relation between a viscous wave's vertical displacement ξ' and the horizontal velocities is modified by at most 6° for the vertical wavelengths greater than 100 m of interest here (Appendix A).

2.4 Summary of commonalities and differences

In the context of Fieberling Guyot, seamount- and vortex-trapped waves share the following properties:

- generation by the barotropic diurnal tide to satisfy the zero-normal-flow bottom boundary condition, so their Eulerian frequencies $\omega_E = \omega_i + nV_\theta/r \simeq \omega_i - \zeta/2 = K_1, O_1$.
- clockwise rotation in time of the horizontal velocity vector above the summit plain such that the radial and azimuthal velocities are 90° out of phase.
- azimuthal propagation clockwise around the seamount (azimuthal mode $n = -1$).
- radial decay away from the seamount.

The differences are more subtle:

- the vortex-trapped wave requires a vortex of sufficient strength to permit a diurnal Eulerian frequency. The conditions for which a

seamount-trapped wave can exist in the presence of a background shear that makes part of the domain effectively superinertial are unclear (Codiga 1996).

- vortex-trapped waves will carry energy and momentum up into the stratified water column. Thus, they can have energy maxima above the bottom (upward energy propagation implies counterclockwise turning of the horizontal velocity vector with depth). Both free and forced seamount-trapped waves are bottom-trapped topographic waves so might be expected to have their maximum signal at the bottom and little turning of the velocity vector with depth. However, subinertial time-dependent benthic Ekman layers also turn counterclockwise with depth and will result in velocity maxima above the bottom (Brink 1995b).
- radial velocity u_r' and temperature T' fluctuations for vortex-trapped waves propagating upward and clockwise around the vortex are in phase to produce a net outward radial heat-flux $\langle u_r' T' \rangle$ (in the absence of forcing and dissipative processes, the divergences of this heat-flux and a nonzero vertical momentum-flux $\langle v_\theta' w' \rangle$ drive a wave-induced mean circulation, \bar{u}_r and \bar{w} , which exactly counterbalances the wave fluxes so there is no net change to the background mean azimuthal flow and density fields). There is no azimuthal heat-flux $\langle v_\theta' T' \rangle$ associated with vortex-trapped modes. For cross-slope standing or propagating inviscid seamount-trapped waves, the radial heat-flux is zero and the azimuthal heat-flux nonzero. These phase relations are only slightly modified by inclusion of eddy viscosity and diffusivity (Appendices A and B).

3. MEASUREMENT AND ANALYSIS TECHNIQUES

3.1 Data

Profiles were collected over the summit and flanks of Fieberling Guyot (32°26'N, 127°45'W) in March 1991 as part of the ONR-sponsored Topographic Interactions program to investigate the impact of seamounts on physical and biological oceanography. Time-series and surveys were made with the High-Resolution Profiler (HRP; Schmitt *et al.* 1988), Sippican expendable current profilers (XCP; Sanford *et al.* 1982; 1993), and Sippican T-5 (1600 m) XBTs. At the seamount's latitude, the Coriolis frequency is $7.8 \times 10^{-5} \text{ s}^{-1}$ (22.4 h) so both the K_1 (24.0 h, 0.933f) and O_1 (25.9 h, 0.865f) diurnal tides are subinertial. Barotropic diurnal tides in this region propagate northwest (Schwiderski 1981a, b).

Fieberling Guyot is the northwestmost member of the Fieberling seamount chain. For the motions above the summit plain discussed here, it appears to be dynamically isolated from its nearest neighbor, Fieberling II, 40 km to the southeast. This is consistent with the conclusion of Roden (1991) that the seamount chain affects background impinging currents as a group only at abyssal depths. Fieberling Guyot rises from an abyssal plain of 4000-4500 m depth to a summit plain at 500-700 m depth (Fig. 1). By definition, a guyot has a flat top (apart from a narrow pinnacle southwest of the geometric center of the summit plain which attains 440-m depth) due to surface wave erosion before sinking of the peak below the surface. Radial bottom slopes on the summit plain are ~ 0.05 compared to flank slopes as high as 0.5. The abrupt change in slope near the 700-m isobath will be referred to as the summit rim. The summit plain is elongated so that the rim radius is about 6.5 km zonally and half that meridionally (Fig. 1). Beyond the rim, Fieberling Guyot can be described as a Gaussian of radial scale 12 km (Codiga 1991).

Other relevant measurements are two mesoscale CTD surveys conducted in August 1989 (Roden 1991) and April - May 1991 (Roden 1994), and year-long current-meter mooring deployments from September 1990 to September 1991 at five sites on Fieberling Guyot and two on the

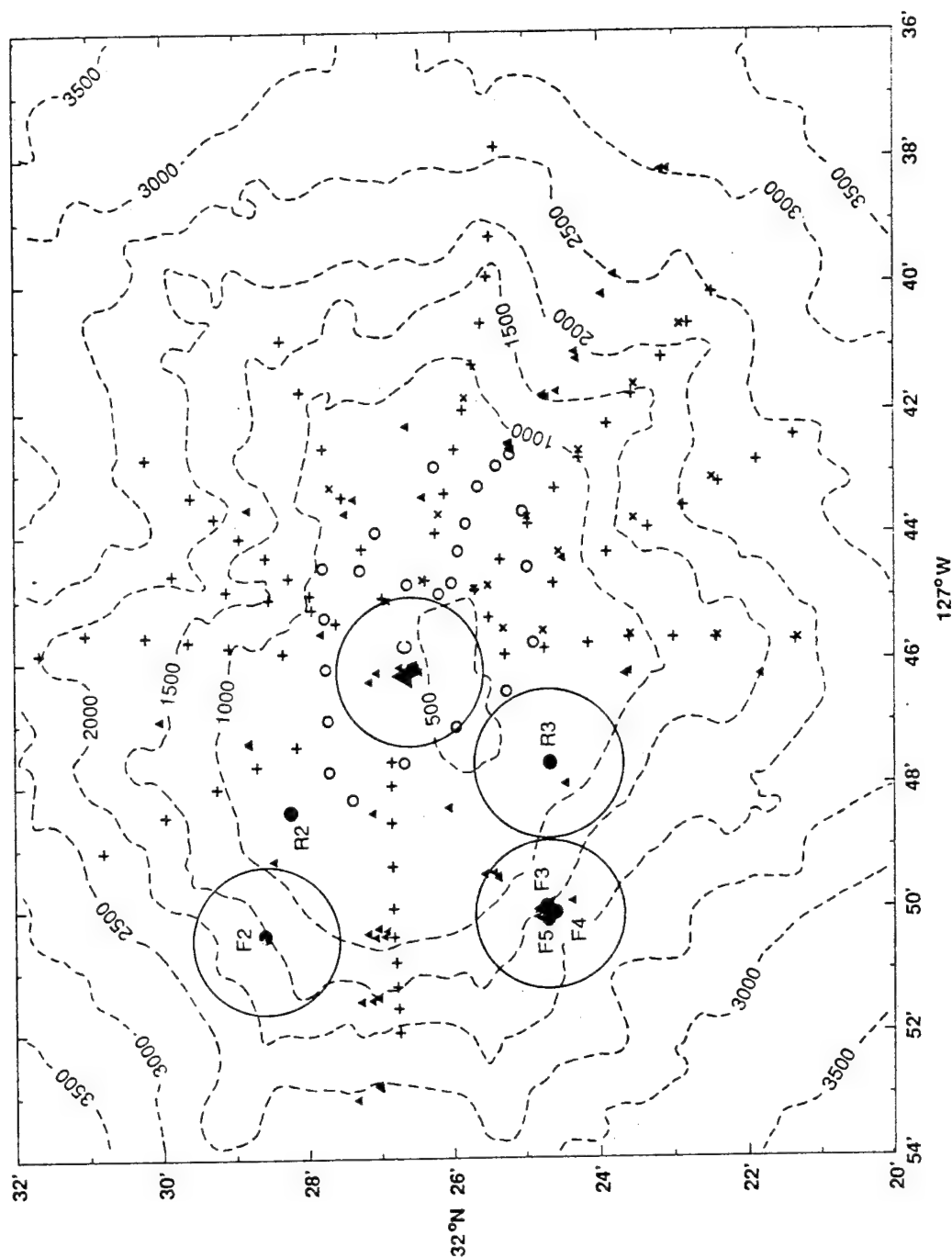


Figure 1: Velocity profiler stations (XCP, +, x, o; HRP, Δ) and current-meter mooring sites (\odot) over the summit plain and flanks of Fieberling Guyot. Bathymetry is in meters. HRP measurements consist of day-long profile time-series at C and F3, spoke time-series to the west and southeast, and a survey around the rim. Radial XCP spokes were made from seamount center to the 2500-m isobath. Surveys to the south and east were collected on 7 March 1991 (+, x), to the north and west on 8 March (+), and on the summit plain on 18 March (o). The circles about all the moorings except R2 denote one-nautical-mile expendable exclusion zones intended to reduce fouling of the current meters by expendable wire.

abyssal plain to the west (Wichman *et al.* 1993; Noble *et al.* 1994; Brink 1995a; Eriksen 1995a, b). Moorings were located at the center of the summit plain (C, Fig. 1), on the rim to the northwest and southwest (R2 and R3), in 1500-m deep water on the flanks to the northwest and southwest (F2 and F3-5) and on the abyssal plain 40 km to the northwest and southwest. The R2 mooring was an upward-looking ADCP while the other moorings were strung with discrete-depth current meters.

The HRP measurements include (i) day-long time-series sampled every 3 h at the central (C) and southwest flank (F3) mooring sites, (ii) repeated radial sections to the 3000-m isobath over the western and southeastern flanks, and (iii) a survey around the rim (Fig. 1). Profiles on the neighboring abyssal plain 20-40 km from the peak are described by Toole *et al.* (1994). The stratified turbulent benthic boundary layer overlying the flanks is examined in Toole *et al.* (1996). The freefall High-Resolution Profiler's (Schmitt *et al.* 1988) sensor suite includes a CTD and a two-axis acoustic current meter which provide finescale vertical profiles of temperature, salinity, pressure and horizontal velocity relative to an unknown but depth-independent constant. Microstructure sensors include a high-speed thermistor, a dual-needle conductivity probe, and airfoil velocity shear probes to estimate microscale temperature and velocity dissipation rates. Schmitt *et al.* (1988) and Polzin (1992) detail reduction of the fine- and microstructure data to 0.5-m depth intervals; the microstructure analysis follows the methodology developed by Neil Oakey at the Bedford Institute of Oceanography. Dissipation rate estimates assume three-dimensional isotropy (Gargett *et al.* 1984). The production/dissipation balances of Osborn and Cox (1972) and Osborn (1980) are used to obtain diapycnal eddy diffusivity estimates employing an upper-bound mixing efficiency of 0.25 (Oakey 1982).

For the seamount cruise, HRP was equipped with a Datasonics, Inc. acoustic altimeter to trigger release of a descent weight when the profiler got within 10 m of the bottom. The weight-release criterion was effective over the summit plain, but less reliable over the steep flanks (presumably because of poor acoustic backscatter). HRP dives frequently terminated up to 100 m above the local bottom and one impacted the bottom.

Most of the XCPs were deployed along radial spokes from near the center of the summit plain to the 2500-m isobath on the flanks (Fig. 1). XCP profiles in water depths less than 1600 m measured into the bottom. A survey of 43 profiles was conducted to the south and east between 0800 and 1300 h on 7 March (+) with 19 of the stations re-occupied between 1330 and 1730 h (x). A survey of 34 profiles was conducted to the north and west between 0500 and 0900 h on 8 March (+). Finally, a survey of 24 profiles was conducted over the summit plain a week and a half later between 0500 and 0830 h on 18 March (o). Most of the XCP data were collected within a few hours of the same phase of the diurnal tide. No expendable probes were dropped within 1 nmi of the moorings to prevent fouling the current-meter rotors with expendable wire. As a result, the southwest quadrant was undersampled.

The expendable current profiler (XCP) measures the horizontal velocity to within an unknown but depth-independent constant using the voltage drop induced by seawater's motion through Earth's magnetic field. Temperature is determined with an XBT thermistor. The maximum measurement depth of the present model is 1600 m. Pre-analysis processing averages the data into 3-m bins with typical rms errors of $\pm 0.4 \text{ cm s}^{-1}$ and $\pm 0.06^\circ\text{C}$ for velocity and temperature, respectively (Sanford *et al.* 1993).

3.2 Analysis

Two features predicted to occur atop a seamount are (i) a vortex cap, which should be axisymmetric and dominantly in azimuthal velocity v_θ , and (ii) a near-bottom intensified azimuthal-mode-one seamount- or vortex-trapped wave forced by the barotropic diurnal tide. The trapped wave should consist of a unidirectional, slightly subinertial jet over the summit which turns clockwise in time (see Fig. 16).

Treating the profile surveys as snapshots, the vortex and wave signals can be separated by azimuthal averaging $\langle \cdot \rangle_\theta$. The coordinate system is centered on the seamount centroid ($32^\circ 26.2' \text{N}$, $127^\circ 45.5' \text{W}$) as determined by Codiga (1991). The unknown barotropic offset is handled by arbitrarily removing the depth-average over 150-300 m depth before azimuthal

averaging. This emphasizes perturbations at and below the summit depth. To compensate for the nonuniform azimuthal sampling (Fig. 1), the azimuthal averages are weighted by the sampling in the N, W, S and E quadrants. This approach works for velocity signals above the summit plain but does not handle the dipolar patterns associated with temperature (vertical displacement). It also does not work below the summit plain depth where topography constrains the flow to be azimuthal and dipolar (Eriksen 1995b). While it might be preferable to fit the data to azimuthal modes as done by Codiga (1996), the present scheme captures the dominant signals above the summit plain and produces results indistinguishable from those of modal fitting. Toole *et al.* (1996) explore averaging relative to local bathymetry orientation.

Averaging the east and north velocities filters out axisymmetric flow, isolating the expected azimuthal-mode-one diurnal wave signal. Azimuthally-averaging azimuthal and radial velocities filters out all azimuthal modes except mode zero, isolating axisymmetric flow. We caution that a vortex cap need not be axisymmetric; numerical simulations do not always find the vortex to be axisymmetric even in the absence of an impinging mean flow (Haidvogel *et al.* 1993). Beckmann and Haidvogel (1996) find that topographic deviations from axisymmetry and bottom roughness have little impact on the zeroth-order dynamics and the horizontal velocity signal but are reflected in the mean density and vertical velocity signatures.

4. THE VORTEX CAP

4.1 Spatial structure

Radial sections of azimuthally-averaged radial velocity $\langle u_r \rangle_\theta$ and azimuthal velocity $\langle v_\theta \rangle_\theta$ are displayed in Fig. 2. The profiles have been WKB-stretched to $N_0 = 5.2 \times 10^{-3} \text{ s}^{-1}$ $[z \rightarrow z'' = \int_z^0 N(z) \cdot dz / N_0]$ to remove variations in the vertical scale and amplitude due solely to changes in the buoyancy frequency N . True depths are indicated along the right axes.

Radial velocities (Fig. 2a) are less than 3 cm s^{-1} over the summit plain ($r < 8 \text{ km}$). The uniformly weak radial flows suggest that our azimuthal averaging scheme is not biased. At some depths, e.g., 580 sm (stretched meters), there is a suggestion of persistent in- or outflow. There is also a hint of a 3 cm s^{-1} inflow below 600-sm depth over the flanks. We hesitate to equate or contrast these with the $1\text{--}2 \text{ cm s}^{-1}$ radial outflow reported near the bottom by Eriksen (1991) and Brink (1995a) because of (i) possible problems with azimuthal nonuniformity, (ii) the short duration of our sampling, and (iii) the profile surveys were collected during a time of relatively weak radial flow based on the R2 ADCP velocities (see Fig. 6).

The average azimuthal velocity (Fig. 2b) displays a much more clearly defined signal. A 200-sm thick layer of anticyclonic flow overlies the summit plain. Maximum speeds of $\sim -10 \text{ cm s}^{-1}$ are found at the rim (radius $r = 7 \text{ km}$). The vortex is bounded above by a 100-m thick $\partial \langle v_\theta \rangle_\theta / \partial z = 1.5 \times 10^{-3} \text{ s}^{-1} = 0.3 \bar{N}$ vertical shear layer and below by a 200-m thick $10^{-3} \text{ s}^{-1} = 0.25 \bar{N}$ shear layer.

Estimates of relative vorticity $\zeta = \partial \langle v_\theta \rangle_\theta / \partial r + \langle v_\theta \rangle_\theta / r$ (Fig. 3) are noisier because they involve derivatives. The vorticity has values of $(-0.50 \pm 0.15)f$ over the summit plain and vanishes over the seamount flanks. In the vortex core, the effective Coriolis frequency $f_{\text{eff}} = f + \zeta = 0.5f = 2\pi / (44.8 \text{ h}) < K_1, O_1$. Freeland (1994) observed a

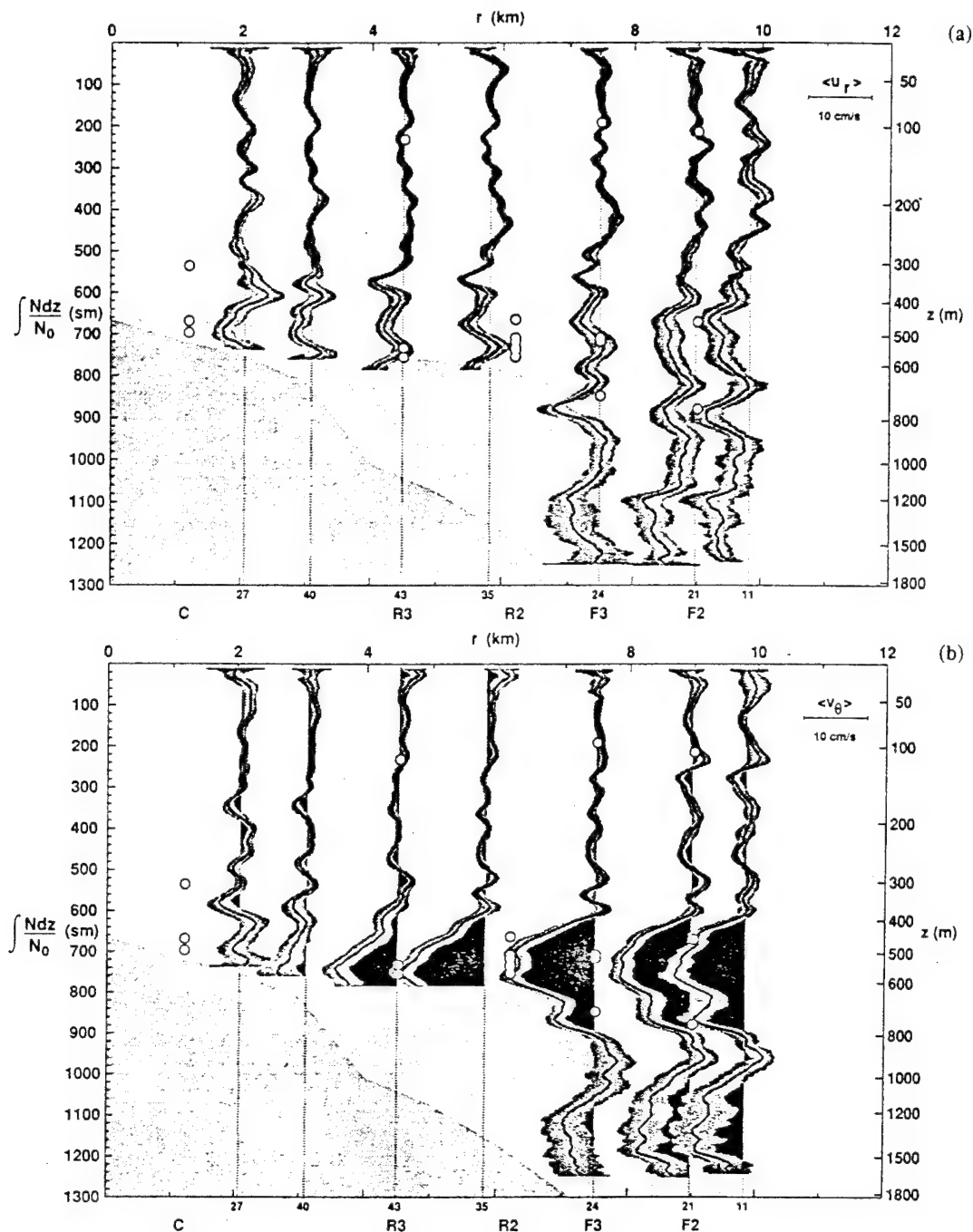


Figure 2: Radial sections of azimuthally-averaged (a) radial velocity $\langle u_r \rangle_\theta$ and (b) azimuthal velocity $\langle v_\theta \rangle_\theta$ with one standard error indicated by dark shading. Nonuniform azimuthal sampling (Fig. 1) is compensated for before averaging. The depth coordinate (left axis) has been WKB-stretched with respect to $N_0 = 5.2 \times 10^{-3} \text{ s}^{-1}$; true depths are shown along the right axis. Numbers along the bottom axis correspond to the number of drops going into each average, darker and lighter silhouettes to extremes in the WKB-normalized bathymetry, and open circles to current-meter sites. The radial velocity $\langle u_r \rangle_\theta$ (a) is everywhere less than 3 cm s^{-1} . The azimuthal velocity $\langle v_\theta \rangle_\theta$ (b) exhibits anticyclonic flow of up to 10 cm s^{-1} over the summit rim at 6-8 km radius between 600 and 900 sm (400- and 800-m depth).

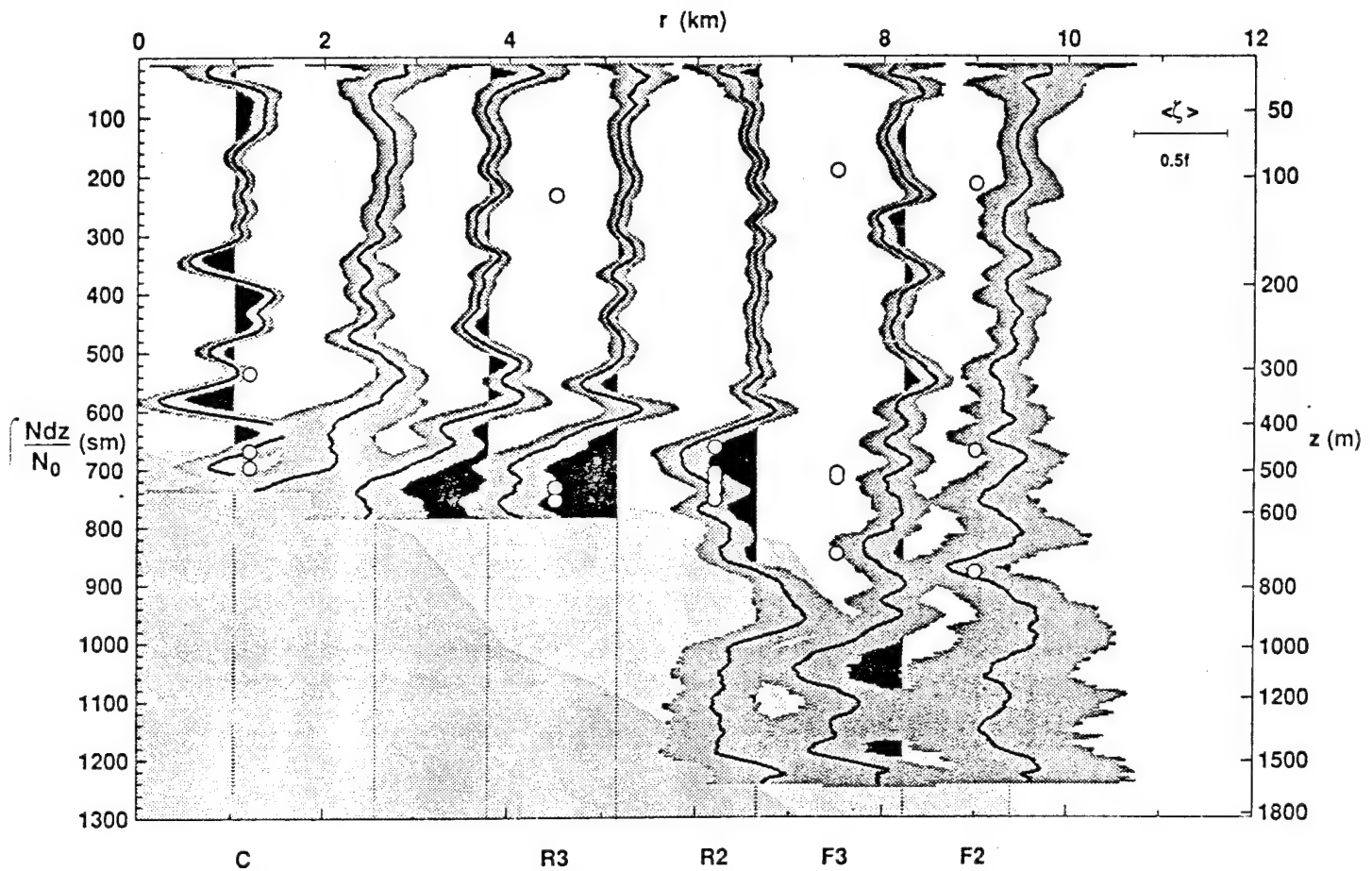


Figure 3: Radial sections of azimuthally-averaged relative vorticity $\langle \zeta \rangle_\theta = \partial \langle v_\theta \rangle_\theta / \partial r + \langle v_\theta \rangle_\theta / r$ with one standard error indicated by dark shading. Relative vorticities of $(-0.50 \pm 0.15)f$ are found in a 200-m thick layer over the summit plain. Vorticities vanish at radii $r > 8$ km, indicating that $\langle v_\theta \rangle_\theta \propto r^{-1}$. Weak vorticity inside 2-km radius may reflect measurement uncertainty in the position of the vortex center.

40-m thick vortex cap of similar strength in ADCP surveys atop Cobb Seamount that was steady on 6-7 day timescales. However, during a later cruise, Codiga (1996) found vorticities weaker than $-0.1f$ over Cobb. There is a hint that the vorticity may vanish inside 2-km radius (Fig. 3), but vortex center position uncertainties are large enough that this cannot be stated conclusively. The absence of a positive vorticity annulus outside the azimuthal velocity maximum indicates that the azimuthal velocity $\langle v_\theta \rangle_\theta$ falls off as r^{-1} for radii $7 < r < 10$ km. As discussed later in connection with the vortex's potential vorticity anomaly, isopycnals are domed over the seamount summit as would be expected for an anticyclonic vortex. Vertical displacements are at most 4 m (see Fig. 7).

4.2 Comparison with current-meter observations

Figures 4 and 5 compare XCP-derived vorticities and azimuthal velocities with centered four-day current-meter averages about the time of the 7-8 March XCP surveys. The current-meter relative vorticity is inferred assuming solid-body rotation, $\zeta = 2\langle v_\theta \rangle_t / r$, where $\langle \cdot \rangle_t$ denotes the four-day average. The current-meter data verify anticyclonic swirling between 400- and 600-m depth (Fig. 4), albeit slightly stronger. The current meters and profilers both find nearly solid-body rotation inside 7-km radius (Fig. 5). Outside the velocity maximum, azimuthal currents fall off more slowly in the current-meter data than in the profiler data. Mean flows shallower than 400 m are weak and show no reluctance to cross isobaths (not shown).

Differences between profiler and current-meter velocities likely arise because the two measurements do not sample the same part of the flow. If the vortex is not perfectly circular, is off center, or is otherwise not axisymmetric, differences in the profiler and current-meter estimates would result. Beckmann and Haidvogel's (1996) simulations produce a vortex with bands of positive relative vorticity localized between R2 and F2, and over the NE flank (their Fig. 8); at other azimuths, little or no positive vorticity is present outside the velocity maximum. Figures 4 and 5 suggest that referencing the XCP velocities to 150-300 m produces offset uncertainties of at worst a few cm/s.

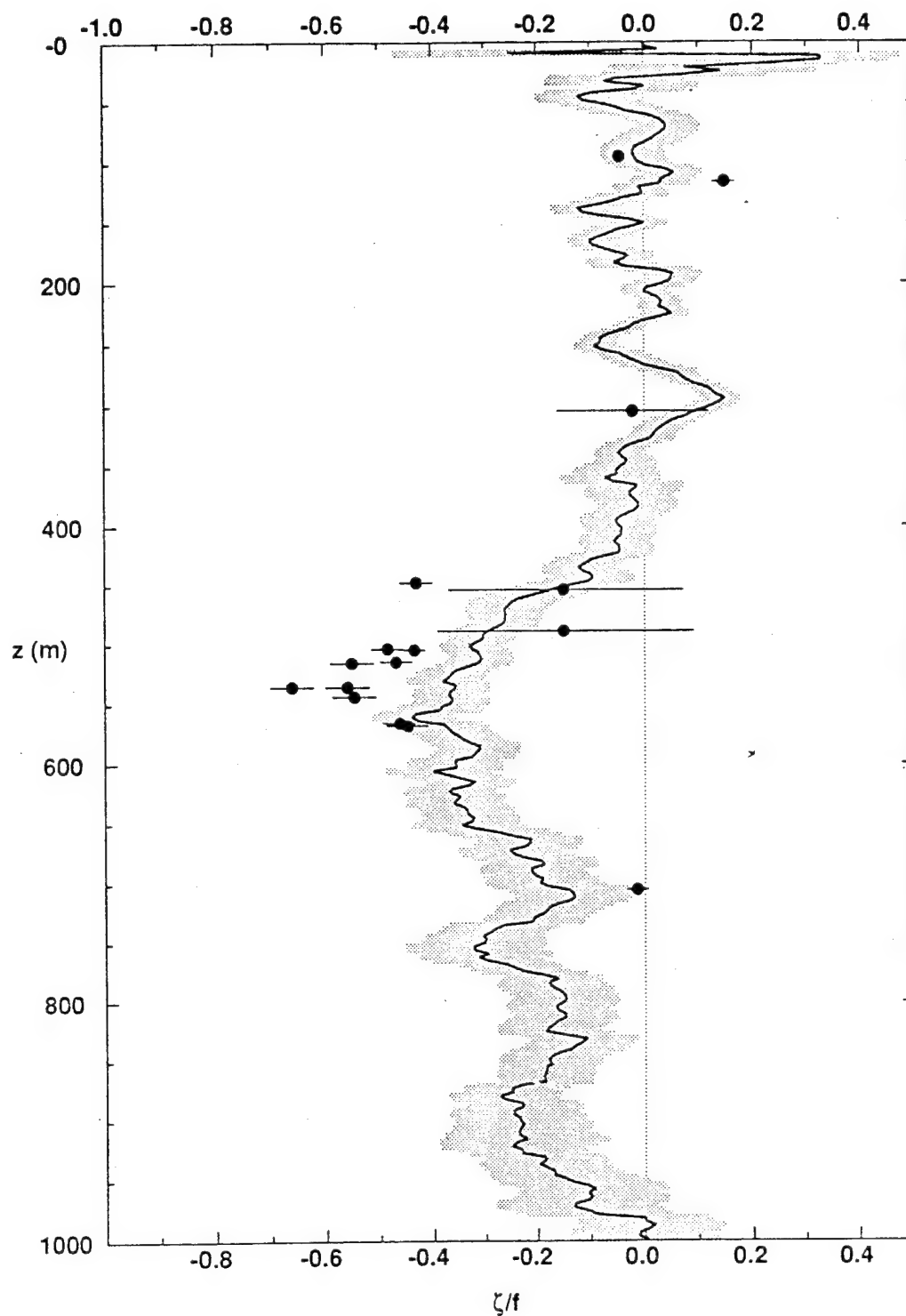


Figure 4: Comparison of the vertical structure of the relative vorticity at $r \approx 6.7$ km from the XCP surveys (solid curve) with four-day smoothed current-meter vorticities inside 7-km radius assuming solid-body rotation, $\zeta \approx 2\langle v_\theta \rangle_t / r$ (\bullet). Standard deviations are shown for each data type. XCP vorticities are $-0.35f$ to $-0.40f$ between 500- and 650-m depth, vanishing abruptly shallower than 400 m and more gradually deeper than 900 m. Current-meter vorticities are slightly stronger at $-0.5f$ to $-0.6f$.

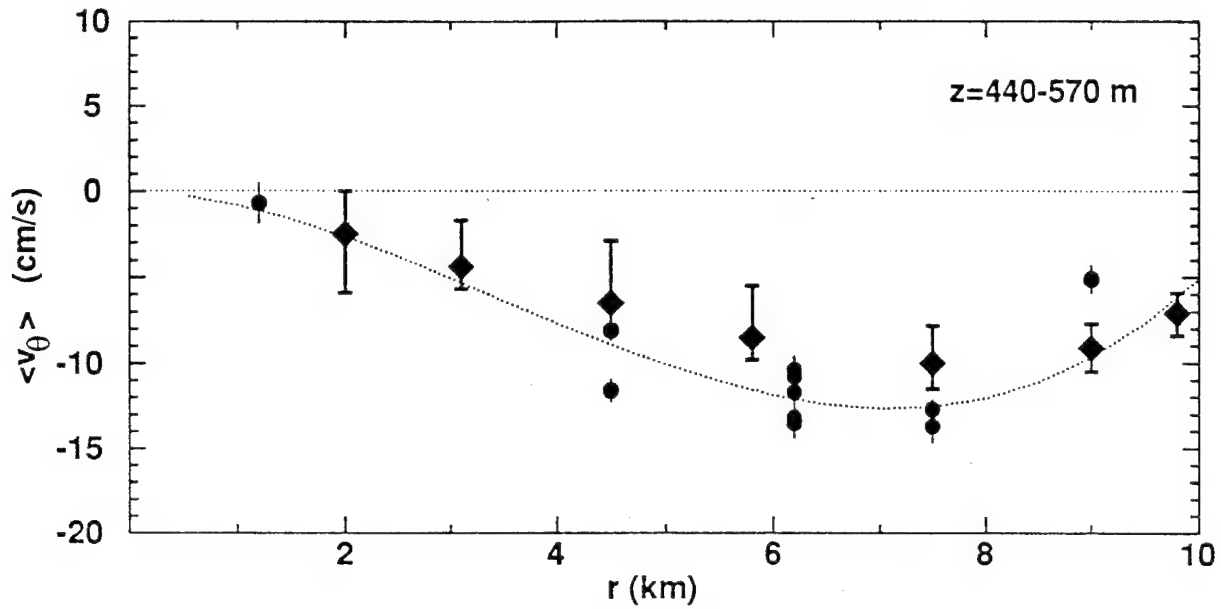


Figure 5: Comparison of the radial dependence of 4-day smoothed current-meter, $\langle v_\theta \rangle_t$ (\bullet), and azimuthally-averaged XCP azimuthal velocities, $\langle v_\theta \rangle_\theta$ (\blacklozenge), in the depth range 440-570 m. The dotted line is a cubic least-squares fit setting $\langle v_\theta \rangle = 0$ at $r = 0$ and $r = 11$ km. The current-meters indicate extreme azimuthal velocities of -14 cm s^{-1} at $r = 6\text{-}7.5$ km with near solid-body rotation at smaller radii. XCPs indicate a similar structure but slightly weaker velocities of $\sim -10 \text{ cm s}^{-1}$.

4.3 Temporal behavior

Fortnightly modulation of vortex strength is apparent in 2-day-smoothed azimuthal velocities from the rim moorings (e.g., spanning 500-750 sm at R2, Fig. 6). This suggests that the vortex cap, with its dome of cold water over the seamount peak, is at least partly sustained against benthic Ekman pumping and turbulent decay by rectification of the K_1 and O_1 tides.

The R2 current-meter time-series also show that the vortex abruptly turns on and off every few months (Fig. 6). Similar behavior is seen at R3. Using the R2 and R3 moorings to obtain time-series of the vortex center position reveal no evidence that the changes in the vortex strength were due to wobbling. Brink (1995a) argues that the vorticity modulation is a function of the impinging zonal flow direction. His Figure 13 shows a tendency for the vortex to be present during eastward and suppressed during westward farfield flow. This is contrary to β -plane dynamics predictions. McCartney (1975) and Verron and LeProvost (1985) find that westward flow produces trapped vortices while eastward flow generates a Rossby wave wake in barotropic β -plane simulations of flow past a small-amplitude seamount. The HRP and XCP measurements were taken at a time of transition from weak eastward to weak westward impinging flow ($\bar{u} \approx \pm 1 \text{ cm s}^{-1}$). Since the vortex flow exceeds the impinging flow, the fluid it contains would be isolated if the flow was steady.

4.4 Potential vorticity anomaly

Though the HRP profiles reveal a 200-m thick positive density anomaly ($\langle \delta \sigma_\theta \rangle = 0.02 \text{ gm cm}^{-3}$, Fig. 7a) associated with the vortex cap (site C, $r \sim 1 \text{ km}$) as compared to flank profiles (F3, $r = 7.5 \text{ km}$), corresponding to an upward vertical displacement of 4 m, it is too weak to produce a discernible buoyancy frequency anomaly. The relative vorticity of the vortex cap thus induces a negative potential vorticity anomaly of $-0.3f\bar{N}^2$ (Fig. 7b) only slightly diminished by the weak positive buoyancy frequency anomaly. The presence of a potential vorticity anomaly is *not* consistent with pure Taylor-Proudman dynamics which preserve potential

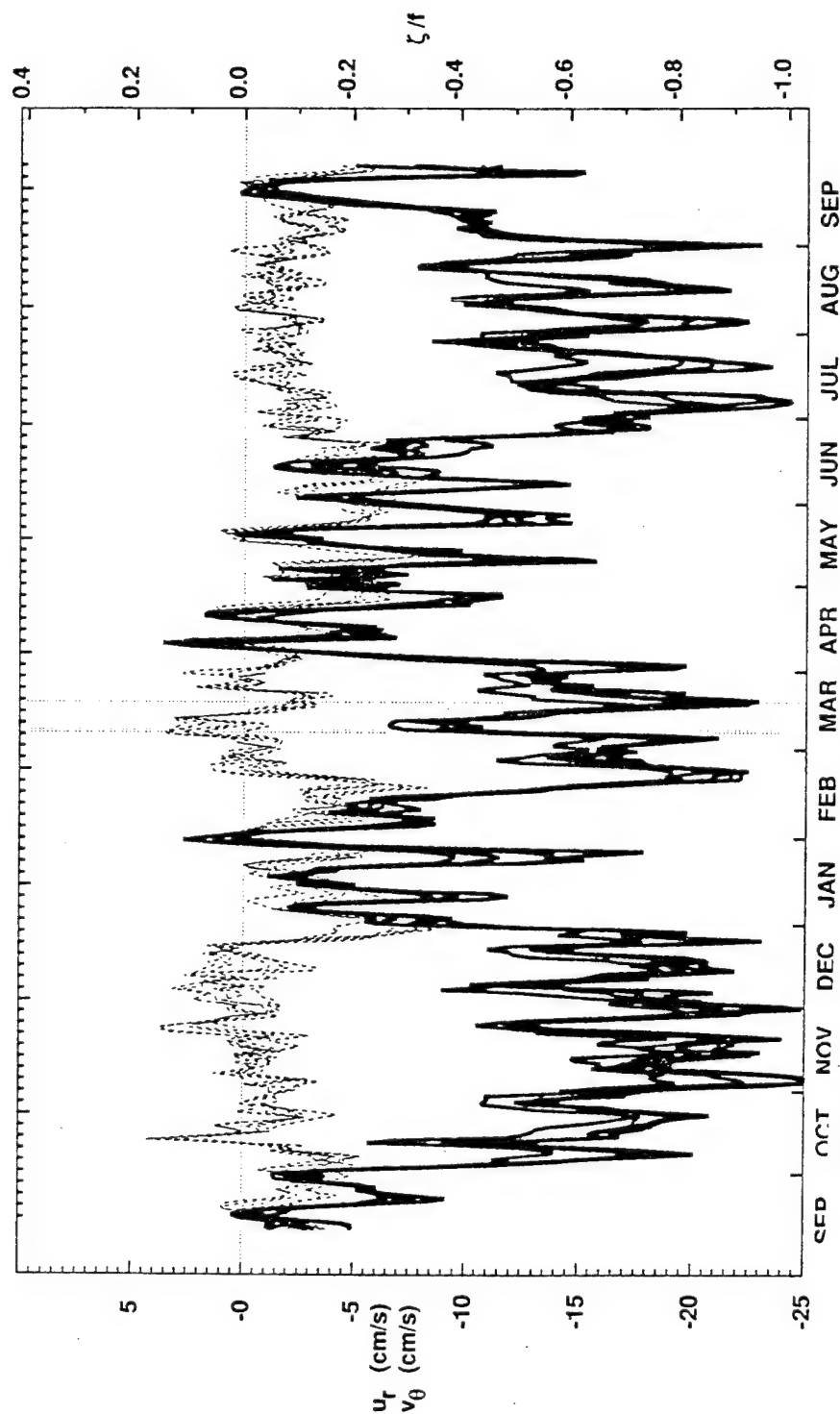


Figure 6: Time-series of 2-day smoothed current-meter azimuthal velocity $\langle v_\theta \rangle_r$ (solid) and radial velocity $\langle u_r \rangle_r$ (dotted) spanning the 500-570 m (700-750 m) depth range of the vortex from the upward-looking ADCP at R2 on the summit plain's rim (Fig. 1). The azimuthal velocity is also expressed as a relative vorticity (right axis) assuming solid-body rotation, $\zeta = 2\langle v_\theta \rangle_r/r$. XCP survey periods are indicated by dotted vertical lines. The radial velocity tends to be less than $\pm 5 \text{ cm s}^{-1}$ while the azimuthal velocity is almost always negative. Fortnightly fluctuations in $\langle v_\theta \rangle_r$ are of insufficient strength to shut off or reverse its direction. Every 2-3 months, the azimuthal velocity abruptly shifts between $\sim 15\text{-}20 \text{ cm s}^{-1}$ and $\sim 5 \text{ cm s}^{-1}$, accompanied by less dramatic changes in the radial velocity.

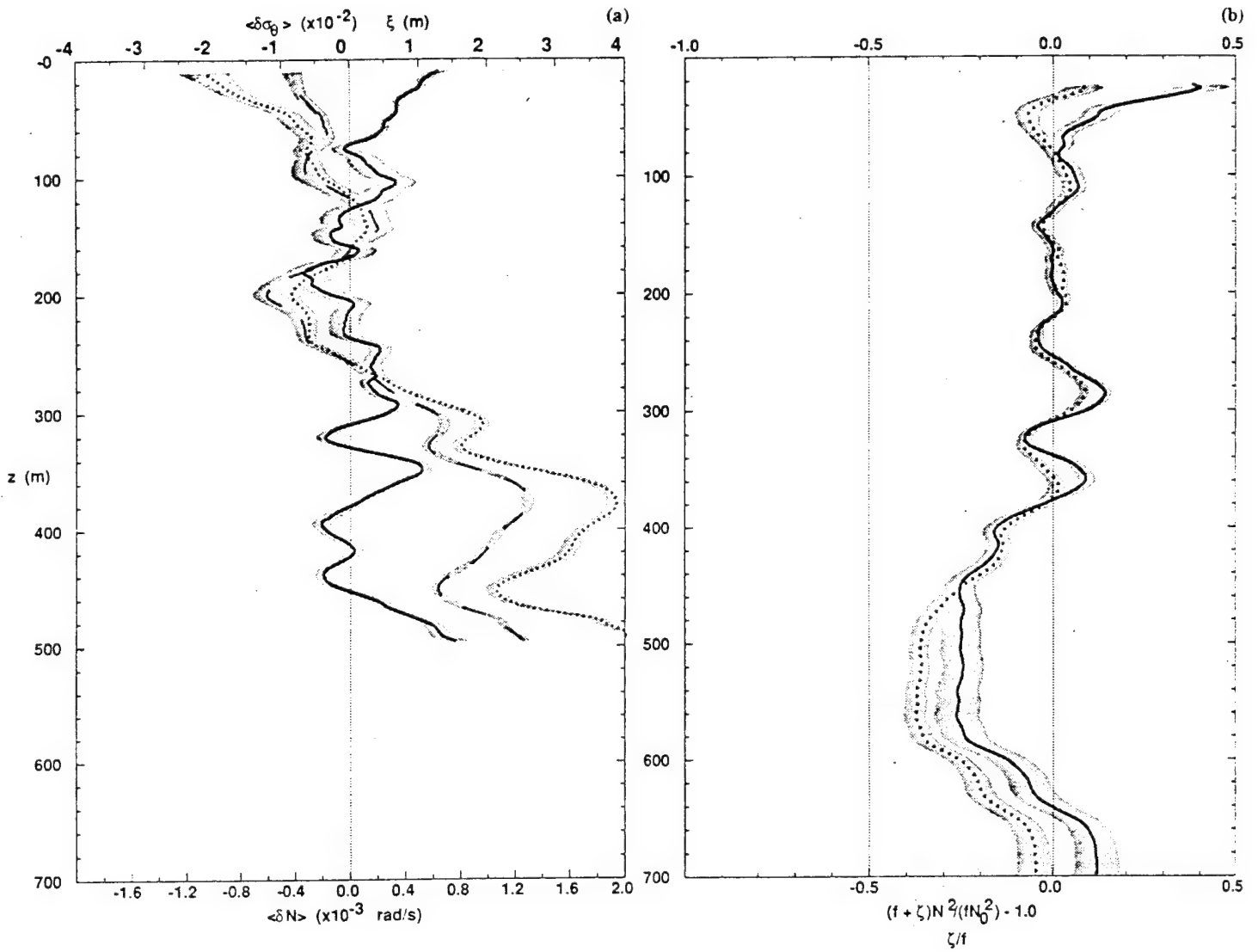


Figure 7: (a) Average HRP density anomaly $\langle \delta \sigma_\theta \rangle$ (dashed), buoyancy frequency anomaly $\langle \delta N \rangle$ (solid) and vertical displacement $\langle \xi \rangle$ (dotted) profiles at site C ($r \sim 1$ km) on the summit plain compared to site F3 7.5-km away on the flanks. The 4-m doming of isopycnals above the summit plain is insufficient to produce a significant buoyancy frequency anomaly. (b) Average profiles of relative vorticity ζ/f (dotted) and potential vorticity anomaly $[(f + \zeta)N_C^2 - fN_{F_3}^2]/fN_{F_3}^2$ (solid) atop the summit plain ($r < 7$ km). The vortex cap has a negative potential vorticity anomaly of $-0.3fN_{F_3}^2$.

vorticity. Viscous damping or bottom friction would produce a *positive* anomaly so cannot account for the observed anomaly. Irreversible forcing or dissipative processes associated with tidal rectification must play a role in creating the negative potential vorticity anomaly.

If features like this potential vorticity anomaly are occasionally shed off seamounts, they might explain the submesoscale potential vorticity anomalies found downstream of Ampere Seamount (Kunze and Sanford 1993).

4.5 Cyclogeostrophic balance

The steady azimuthally-averaged radial momentum equation can be expressed

$$\boxed{\frac{V_\theta^2}{r} + fV_\theta = \frac{\partial P}{\partial r}} + \frac{\partial \langle u_r'^2 \rangle}{\partial r} + \frac{\langle u_r'^2 \rangle - \langle v_\theta'^2 \rangle}{r} + \frac{\partial \langle u_r' w' \rangle}{\partial z} \quad (3)$$

where the reduced, or kinematic, pressure $P = P/\rho_0$, P is the dynamic pressure and the neglected radial acceleration $\partial U_r/\partial t$ is at most 5% of the Coriolis acceleration. The boxed terms are the cyclogeostrophic (gradient-wind) balance expected for steady inviscid flow with curvature in the absence of strong forcing, e.g., rings and Meddies. Beckmann and Haidvogel (1996) find only 15% deviations from balance in their numerical simulations. We will refer to the lefthand side of (3) as the *effective Coriolis acceleration*. The unboxed terms on the right represent momentum-flux-divergence forcing by fluctuating velocities. Figure 8 compares the right- and lefthand sides of a radially-integrated cyclogeostrophic balance

$$\int_r^{r_0} \left[\frac{V_\theta^2}{r} + fV_\theta \right] \cdot dr = \delta P = \int_z^{200 \text{ m}} \delta B \cdot dz \approx g \frac{\partial \sigma_\theta}{\partial T} \int_z^{200 \text{ m}} \delta T \cdot dz, \quad (4)$$

making use of the hydrostatic balance, $\partial P/\partial z = B$, and the local T, σ_θ -relation, $\partial \sigma_\theta/\partial T$, to infer pressure anomalies δP from the XCP-derived temperature anomalies δT relative to the outermost radial bin at $r_0 \sim 10$ km. The vertical integral is taken downward from the center of our 150-300 m level-of-no-

FIEBERLING XCP

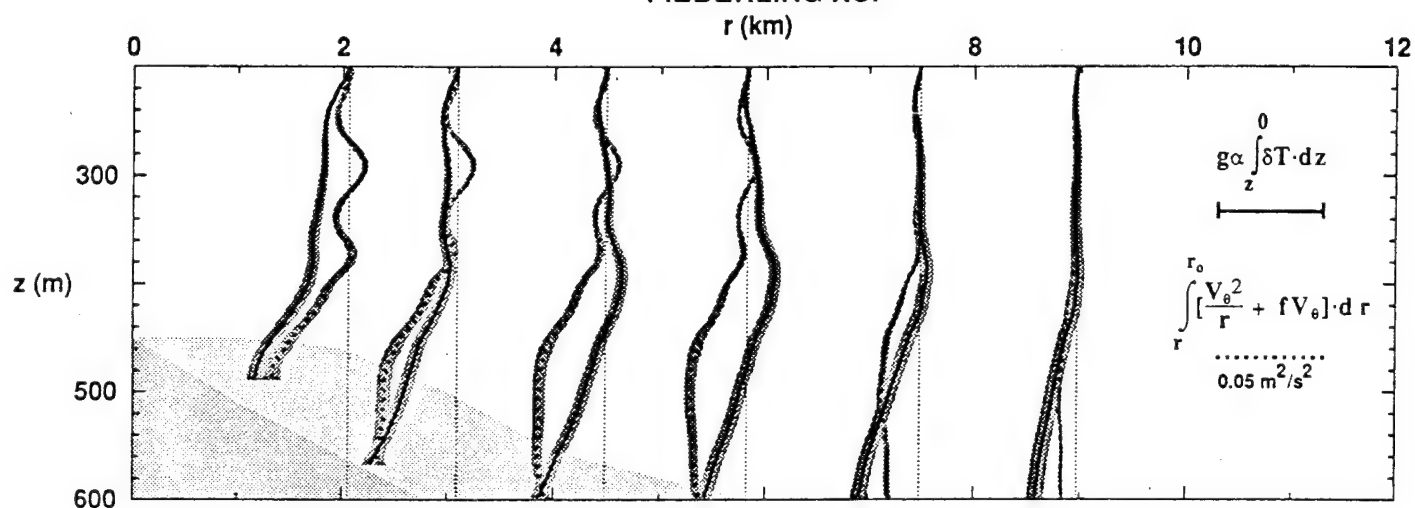


Figure 8: Comparison of the radially-integrated mean effective Coriolis

acceleration $\int_r^{r_o} \left[\frac{\langle v_{\theta} \rangle_{\theta}^2}{r} + f \langle v_{\theta} \rangle_{\theta} \right] \cdot dr$ (dotted) with the mean pressure

anomaly $\delta p = g \frac{\partial \sigma_{\theta}}{\partial T} \int_{z_o}^z \langle \delta T \rangle_{\theta} \cdot dz$ (solid) as a test of the cyclogeostrophic

(gradient-wind) balance (3) where $r_o = 10$ km and $z_o = 200$ m. The quantities are comparable above the summit plain for radii $r < 4$ km. But pressure anomaly and effective Coriolis acceleration have different vertical structures for $r > 4$ km.

motion. The effective Coriolis acceleration terms result in a negative anomaly between 400- and 600-m depth (dotted curve in Fig. 8). At radii $r < 4$ km, the pressure anomaly δP in this depth range (solid curve) is of the same sign and comparable magnitude, so the vortex cap appears to be in cyclogeostrophic balance. For larger radii, the magnitudes of the two sides of (4) remain comparable but the vertical structure differs. The discrepancy becomes even greater below 600-m depth (not shown), where a growing negative pressure anomaly has no balancing signal from the effective Coriolis acceleration. This discrepancy is seen independently in both XCP and HRP data, and is also found in Beckmann and Haidvogel's (1996) numerical simulation. The horizontal momentum-flux divergences on the righthand side of (3) cannot account for it, making at most a 10% contribution. The vertical momentum-flux divergence contribution might be estimated from $\langle u_r'^2 \rangle \sim 2 \times 10^{-3} \text{ m}^2 \text{ s}^{-2}$ and the bottom slope α_0 by recognizing that there can be no flow into the bottom so the ratio $w'/u_r' = \alpha$ is identical to the bottom slope α_0 at the bottom, and that this constraint relaxes away from the bottom. For the sake of argument, assume $\alpha = \alpha_0 \cdot \exp[(z - z_b)/(z_b - z_0)]$ relaxing on a depth scale $z_b - z_0$ over which the imbalance is observed, where z_b is the water depth on the flanks and z_0 the depth of the summit plain. Then

$$\int_r^{r_0} \frac{\partial \langle u_r' w' \rangle}{\partial z} \cdot dr = \int_r^{r_0} \frac{\partial (\alpha \langle u_r'^2 \rangle)}{\partial z} \cdot dr .$$

Plugging numbers into these assumptions, the vertical momentum-flux divergence is only a few percent of the imbalance so is unable to account for the observed discrepancy at $r > 4$ km. Reasonable alternative relations for α yield similar results.

The sole remaining plausible explanation for the discrepancy is that the azimuthal sampling is inadequate to filter out the dipolar horizontal temperature structure of the diurnal wave. Over the flanks, there are no XCP data in the SW quadrant. In an extreme case, this would make it impossible to distinguish between an azimuthally-uniform contribution and a

dipole with an extremum in that quadrant. We conclude that the unbalanced pressure anomaly δP at radii $r > 4$ km and depths $z > 400$ m is likely due to sampling bias.

5. DIURNAL SHEAR

5.1 Temporal behavior

Current-meter time-series (Genin *et al.* 1989; Eriksen 1991; Noble *et al.* 1994; Brink 1995a) have established that there is a $\pm 15 \text{ cm s}^{-1}$ diurnal oscillation atop the summit plain of Fieberling Guyot with large contributions from both K_1 (0.933 f) and O_1 (0.865 f) tidal frequencies. Both are 100 times more energetic than the barotropic tides in the far field, with K_1 about four times more energetic than O_1 . Beating of these two tidal constituents produces a subharmonic fortnightly cycle and a harmonic at M_2 (of magnitude $\delta T = 0.28^\circ\text{C}$). The dominance of the diurnal frequency is confirmed by the day-long HRP profile time-series at C and F3 though the tidal constituents could not be separated. Grayscale HRP time-series at sites C and F3 (Fig. 9) reveal clockwise rotation of the velocity vector in time and counterclockwise rotation with depth (downward phase propagation) between 300- and 600-m depth. Dropped lag coherences for vertical wavelengths $\lambda_z = 32\text{-}128 \text{ m}$ imply a period of 23.6 h (0.95 f). The dominant diurnal signal in the flank profile time-series is isolated by several hundred meters from the bottom.

Vertical isopycnal excursions of $\pm 20 \text{ m}$ are observed in the center and flank HRP time-series (Fig. 9) with similar vertical and temporal scales as those found in velocity. Their downward phase propagation over the flank leads us to conclude that the step-like structures seen in individual temperature and salinity profiles are produced by diurnal straining, not turbulent mixing. At site C on the summit plain, the vertical displacement field is dominated by semidiurnal harmonics.

5.2 Spatial structure

Azimuthally averaging the east and north velocities in the XCP snapshots filters out axisymmetric flow associated with the vortex and isolates azimuthal-mode-one structure associated with the diurnal oscillations above the summit plain. Diurnally backrotating the profiles to a common time before averaging did not capture significantly more variance because

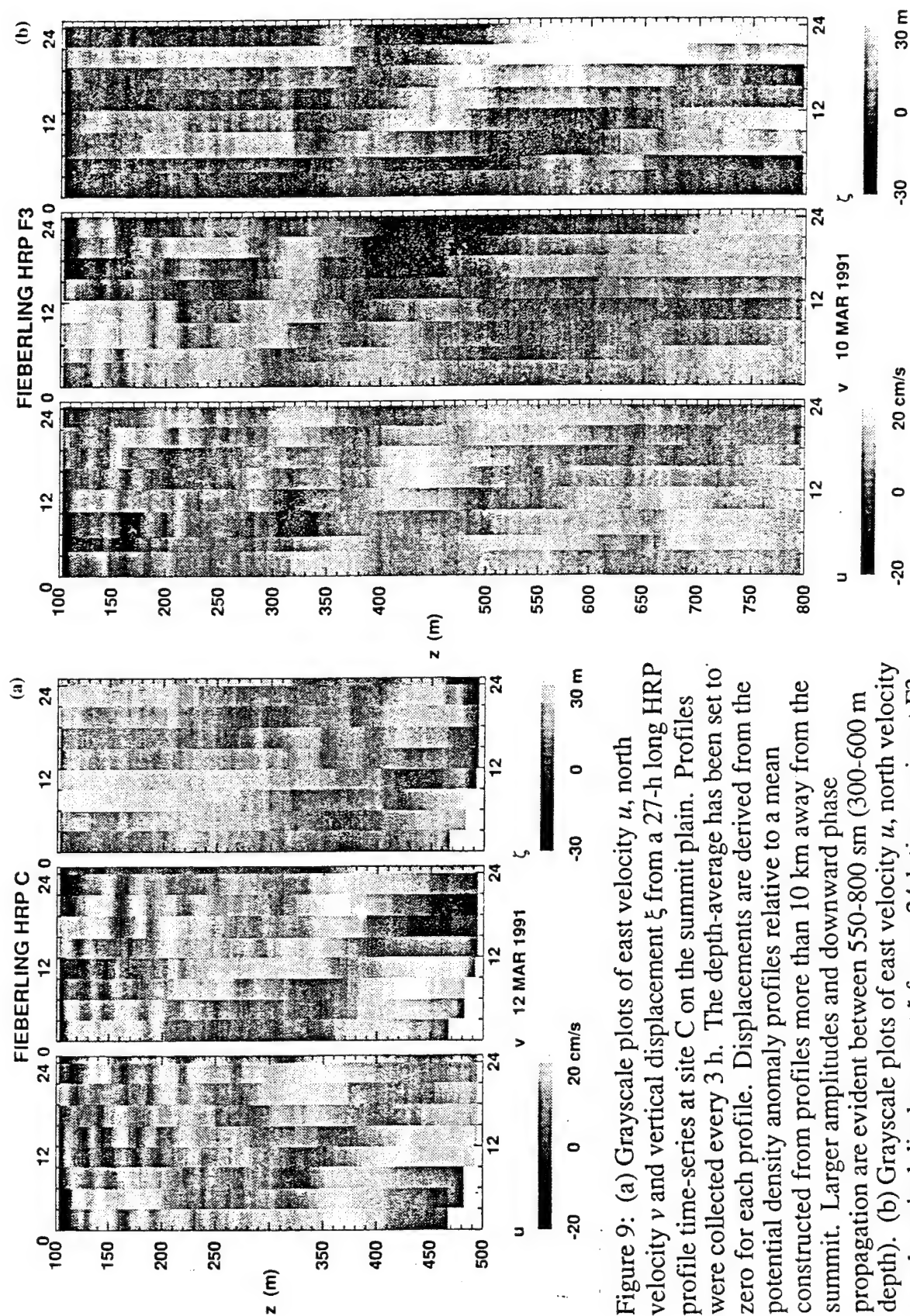


Figure 9: (a) Grayscale plots of east velocity u , north velocity v and vertical displacement ξ from a 27-h long HRP profile time-series at site C on the summit plain. Profiles were collected every 3 h. The depth-average has been set to zero for each profile. Displacements are derived from the potential density anomaly profiles relative to a mean constructed from profiles more than 10 km away from the summit. Larger amplitudes and downward phase propagation are evident between 550-800 m (300-600 m depth). (b) Grayscale plots of east velocity u , north velocity v and vertical displacement ξ from a 24-h time-series at F3 on the flank. Local bottom depth is ~ 1500 m.

the XCP profiles were all collected within a few hours of the same phase of the diurnal tidal forcing.

Radial sections of azimuthally-averaged, WKB-normalized east and north velocity, $\langle u \rangle_\theta$ and $\langle v \rangle_\theta$, are displayed in Fig. 10. Because of the fixed vertical resolution of the measurements, WKB-stretching produces higher stretched vertical resolution where N is small, accounting for the smaller apparent vertical scales deep than shallow. A 150-sm thick layer of intensified east and north velocity ($\pm 15 \text{ cm s}^{-1}$) is evident immediately above the summit plain (550-700 sm, 350-500 m). The signal decays on 3-4 km radial scales away from the summit but is still visible at 10-km radius.

The efficacy of the averaging scheme in isolating the bulk of the variance above the summit plain is demonstrated in Fig. 11. Between 550- and 650-sm depth, the variance in the average (a) exceeds that in the residual (b) by a factor of two. At other depths, the residual contains more variance than the average, indicating that azimuthal-mode-one structure dominates only immediately above the summit plain. Maximum average velocities exceeding 15 cm s^{-1} lie between 600 and 650 sm (400 and 450 m), about 100 m above the bottom inside 2-km radius. Velocity maxima about 170 m above the bottom at ~ 450 -m depth are seen at the rim. Maxima above the bottom could be consistent with either the vortex-trapped wave scenario or seamount-trapped oscillations with a benthic Ekman layer.

The relatively low variance in both the average and residual between 150- and 500-sm depth is a consequence of assuming a level of no motion in that depth range. This will result in excess variance below the summit depth, particularly in the residual (Fig. 11b).

The diurnal shear layer (Fig. 10) is present in both east and north velocities but is out of phase in the vertical in the sense that the velocity vector turns counterclockwise with depth. This can be seen most clearly in Fig. 12, which displays a radial slice of the orientation of the horizontal velocity vector, $\theta = \text{Arctan}(\langle v \rangle_\theta / \langle u \rangle_\theta)$, in the depth range 500-800 sm (300-600 m) where the signal is most energetic. The velocity vector orientation θ increases monotonically with depth by 240° in 150 sm. This

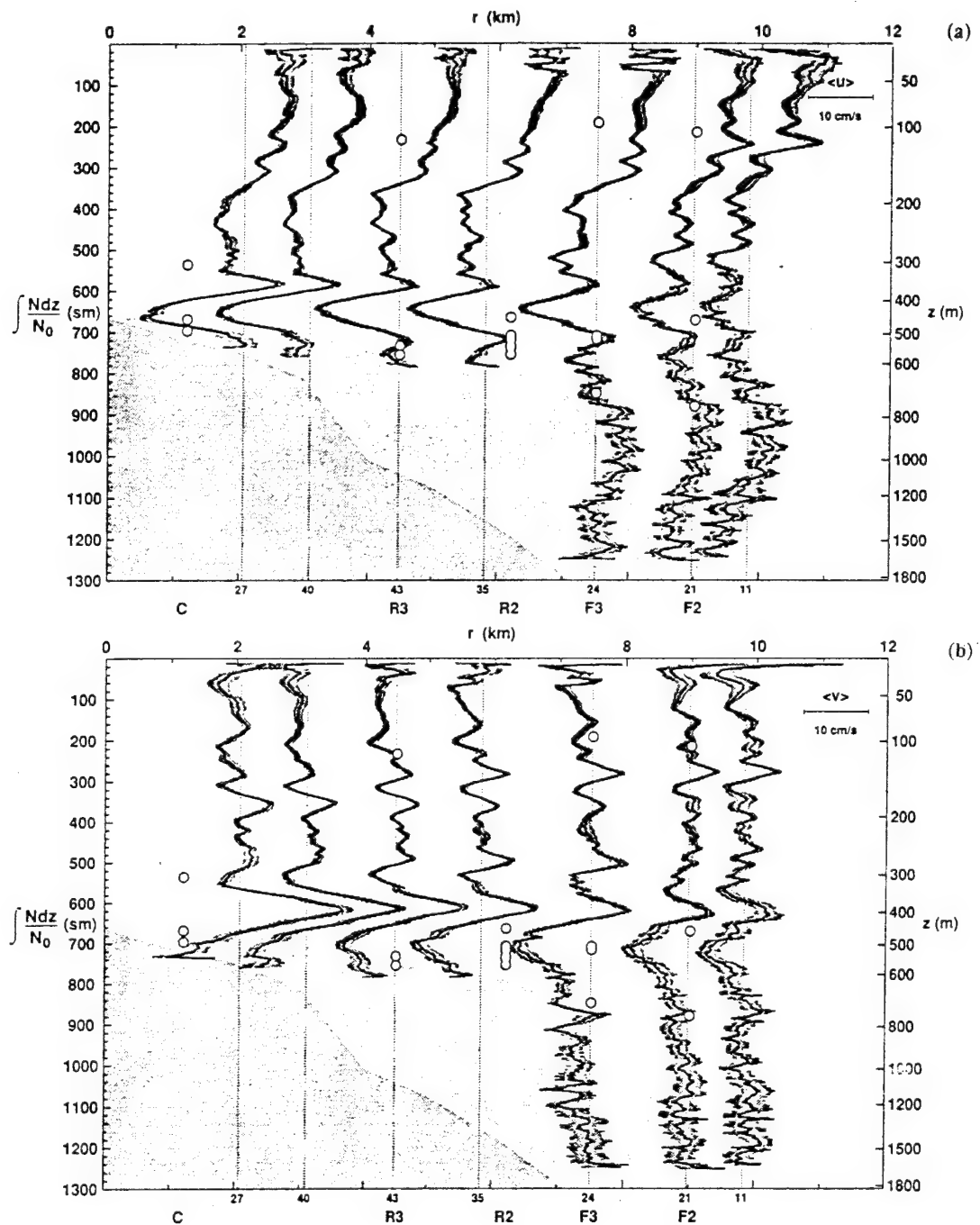


Figure 10: Radial sections of azimuthally-averaged, WKB-normalized east velocity $\langle u \rangle_\theta$ (a) and north velocity $\langle v \rangle_\theta$ (b) over the summit plain and flanks. Shading about the profiles indicates one standard error. WKB-stretched depths are indicated along the left axis and true depths along the right axis. Light and dark silhouettes indicate extremes of bathymetry, open circles the locations of current-meters, and numbers at the bottom the number of drops going into each average. A 150-sm thick layer of 10-15 cm s⁻¹ velocities lies 50-100 sm above the summit plain and rim, evanescent radially away from the seamount. Extrema in $\langle u \rangle_\theta$ and $\langle v \rangle_\theta$ are not at the same depths but offset in the sense that the velocity vector turns counterclockwise with depth (see Fig. 12 and 13). There is also a horizontally-coherent wave of $\lambda_z = 50$ sm in $\langle v \rangle_\theta$ but not $\langle u \rangle_\theta$ between 200- and 400-sm depth.

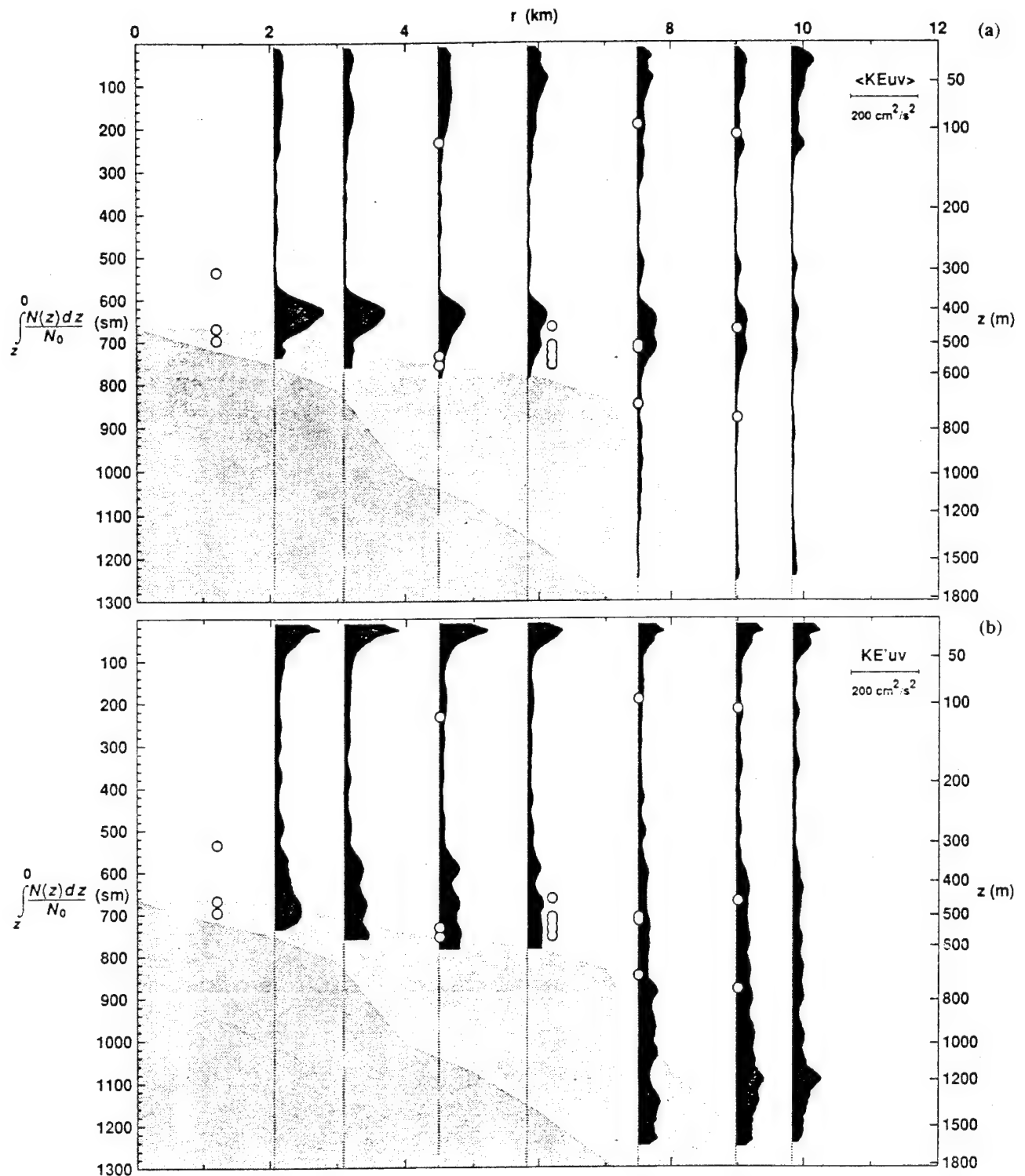


Figure 11: Radial sections of WKB-normalized (a) average Cartesian kinetic energy $\langle KE_{uv} \rangle_\theta = (\langle u \rangle_\theta^2 + \langle v \rangle_\theta^2)/2$ and (b) residual kinetic energy $KE'_{uv} = \langle u^2 + v^2 \rangle_\theta/2$. The average kinetic energy (a) has a peak exceeding $100 \text{ cm}^2 \text{ s}^{-2}$ between 600- and 700-sm (400-500 m depth), 50-100 sm above the summit plain. The residual kinetic energy (b) has more uniform overall energies with no well-pronounced peak above the summit, demonstrating the efficacy of the averaging scheme in isolating the feature over the summit plain. The larger residual energy below 500-sm depth is due to removal of 150-500 sm velocities from the profiles before azimuthal averaging. Residual energy dominates over the flanks below the summit depth.

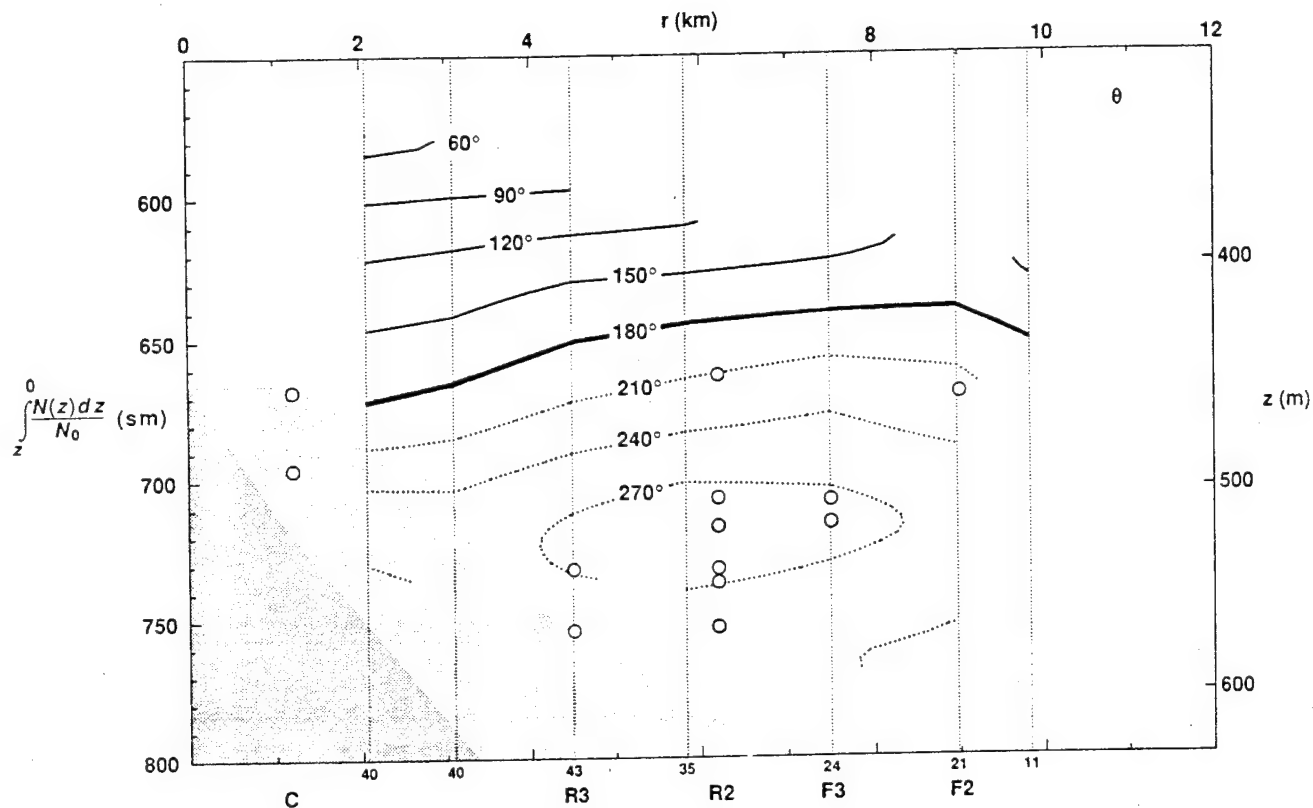


Figure 12: Radial section of the orientation of the azimuthally-averaged Cartesian horizontal velocity, $\theta = \text{Arctan}(\langle v \rangle_\theta / \langle u \rangle_\theta)$, in the shear layer (Fig. 10). The orientation θ is only contoured where the horizontal kinetic energy exceeds $15 \text{ cm}^2 \text{ s}^{-2}$. The increase of the orientation θ by 240° from 580- to 720-sm depth is a consequence the velocity vector turning counterclockwise with depth. The corresponding vertical wavelength is $\sim 210 \text{ sm}$. The sense of the turning is consistent with (i) near-inertial waves of upward energy propagation or (ii) subinertial time-dependent bottom Ekman spirals. The orientation θ also increases by 30° in 6-km radius.

uniform vertical gradient is also seen in the upward-looking ADCP measurements in the bottom 50 m at R2 (Fig. 13). XCP profiles show that it extends over a depth range four times greater than predicted by Brink's (1990) model (Fig. 13). While the depth of the velocity reversals in Brink's seamount-trapped wave model varies azimuthally and in time, the smooth turning evident in the averages (Figs. 12 and 13) is also typical of individual XCP and HRP profiles; no 180° reversals were observed.

If interpreted as a near-inertial internal wave, the orientation θ is a measure of wave phase. The observed gradient $\partial\theta/\partial z$ ($\equiv k_z$) corresponds to a vertical wavelength $\lambda_z \approx 210$ m. The counterclockwise turning with depth implies downward phase and upward energy propagation. The orientation also increases by 30° in 5-7 km radius (Fig. 12), consistent with a radial wavelength of ~ 80 km for planar geometry. For an internal wave, energy propagates along lines of constant phase in the vertical plane so the orientation contours would be interpreted as outward as well as upward energy propagation.

The dependence of the vertical turning wavelength λ_z ($= 2\pi/k_z$) on relative vorticity can be inferred from the year-long R2 ADCP mooring records. Fits at each depth bin of a diurnal oscillation plus a mean were made to two-day segments of the velocity records at depths of 660-750 m (450-570 m). The relative vorticity was estimated from the two-day-average mean azimuthal velocity assuming solid-body rotation, $\zeta = 2\langle V_\theta \rangle / r$. The vertical turning wavelength was inferred from vertical linear fits to the orientation of the diurnal velocity signal weighted by the clockwise-in-time diurnal kinetic energy, that is, minimizing $\sum_{i=1}^N KE_{CW_i}(\theta_i - k_z z_i - \theta_0)^2$ with respect to k_z and θ_0 . Examination of individual orientation profiles showed them to be generally linear with depth in the counterclockwise-with-depth sense, particularly for vorticities stronger than $-0.3f$.

The results are summarized in Fig. 14 which displays the inferred vertical turning wavelength λ_z and clockwise-in-time diurnal kinetic energy versus relative vorticity ζ/f . The vortex-trapped wave model prediction (1)

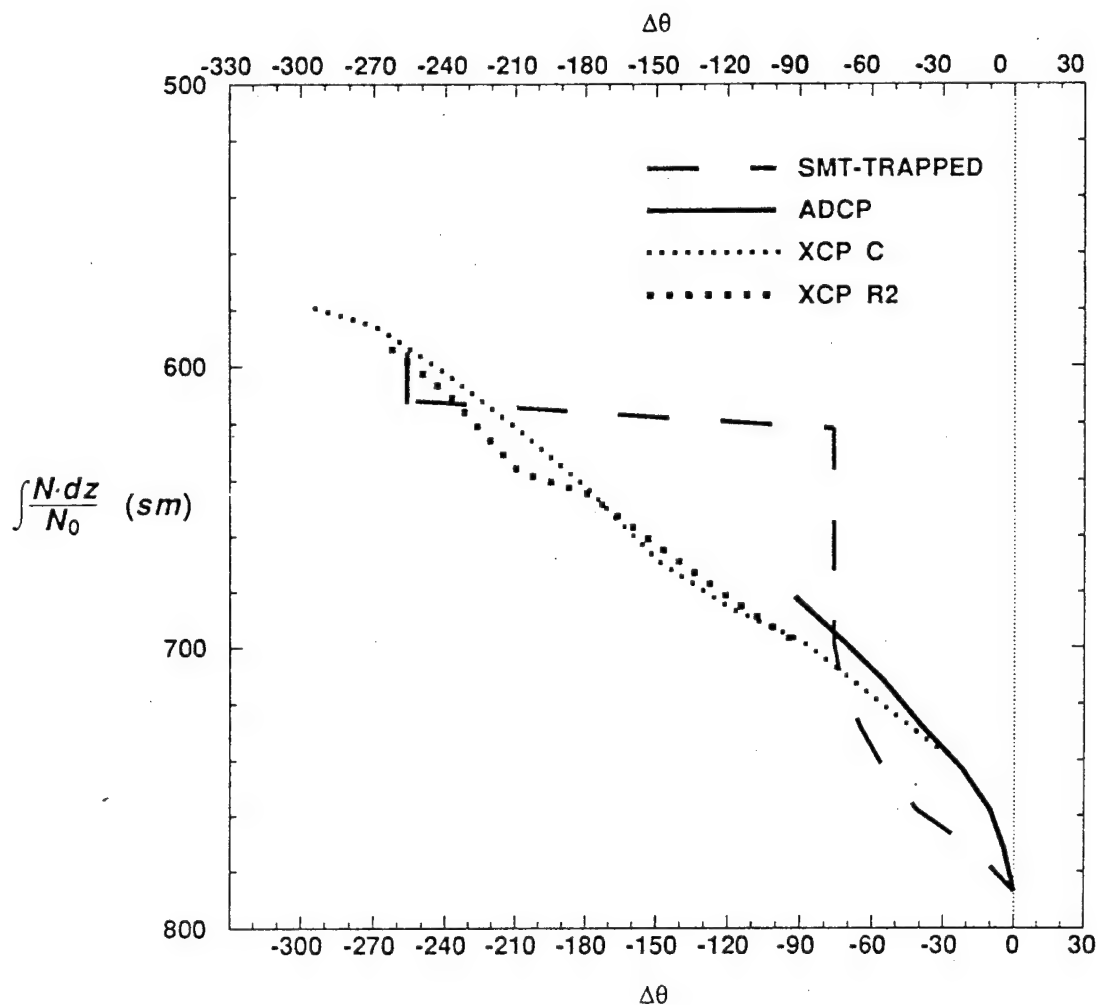


Figure 13: Comparison of the velocity orientation $\Delta\theta$ as a function of WKB-stretched depth from Brink's (1990) seamount-trapped wave model (dashed), the rim R2 ADCP mooring (solid), and XCPs near the center and on the rim of the summit plain (dotted). XCP and ADCP gradients are roughly consistent in the overlapping depth range 680-780 sm. The model's bottom spiral is also roughly consistent with the turning in this depth range. However, the XCP profiles indicate that the phase gradient θ_z extends to 580-sm depth while the seamount-trapped wave model indicates uniform phases above 700 sm until 620-sm depth, then a 180° phase shift (velocity reversal) at shallower depths.

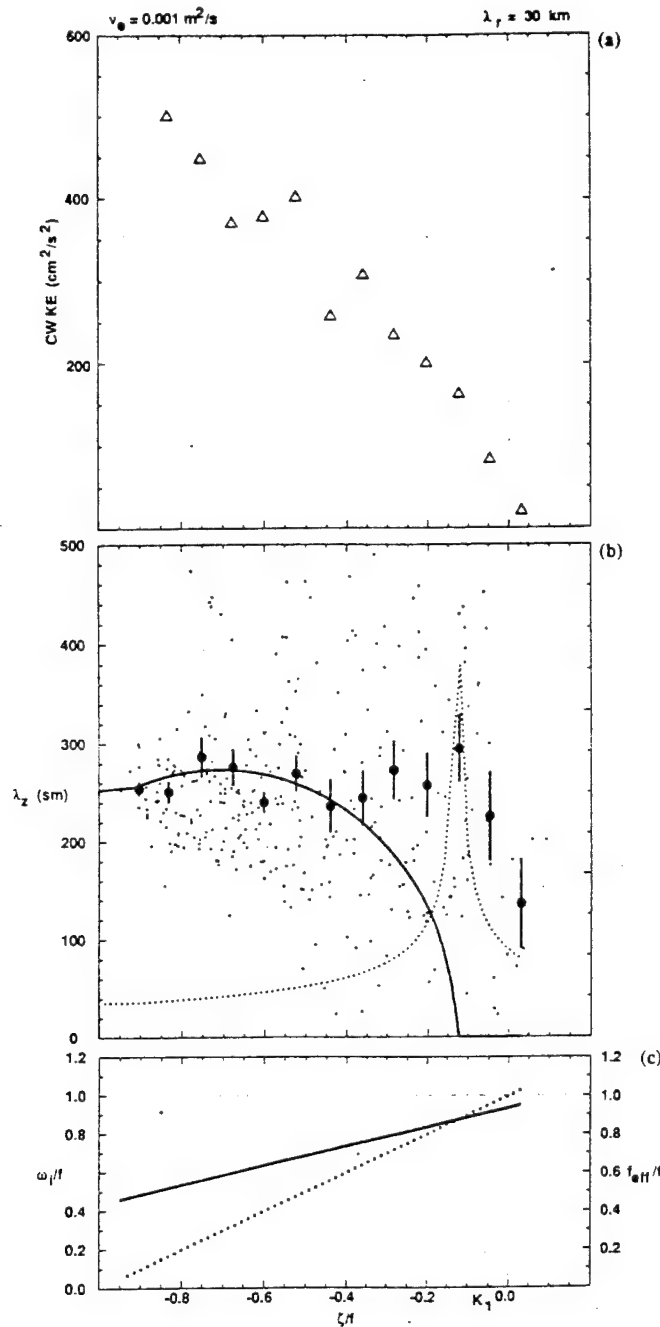


Figure 14: (a) Clockwise-in-time diurnal kinetic energy from 2-day fits of diurnal sinusoids to the rim ADCP records. The energies are binned with respect to relative vorticity. Larger diurnal signals and strong negative vorticities are associated with each other. (b) Dependence on relative vorticity of vertical wavelengths λ_z inferred from the counterclockwise turning of the diurnal horizontal velocity vector with depth (small dots in middle panel). Large dots are bin averages with 95% confidence limits. Solid and dotted curves are the vortex-trapped wave vertical wavelength (2) for fixed radial wavelength $\lambda_r = 30 \text{ km}$, and the larger root for the time-dependent benthic Ekman layer turning wavelength (1) using an eddy viscosity $\nu_e = 10 \times 10^{-4} \text{ m}^2 \text{ s}^{-1}$. The average observed wavelength of $250 \pm 20 \text{ m}$ matches the vortex-trapped wave model prediction for vorticities stronger than $-0.35f$. (c) The intrinsic frequency $\omega_i = K_1 + \zeta/2$ (solid) and effective Coriolis frequency $f_{eff} = f + \zeta$ (dotted) as functions of relative vorticity.

for a fixed radial wavelength $\lambda_r = 30$ km (from Fig. 17) is displayed as the solid curve. The larger root of the time-dependent benthic Ekman layer turning wavelength (2) is shown as the dotted curve using an eddy viscosity $V_e = 10 \times 10^{-4} \text{ m}^2 \text{ s}^{-1}$ consistent with the microstructure data and a turbulent Prandtl number of one. The Ekman turning wavelength has a maximum at an intrinsic frequency $\omega_i = \omega_E + \zeta/2 = f_{eff} = f + \zeta$, or $\zeta = 2(\omega_{K_1} - f)$. For vorticities $\zeta < -0.35f$, the observed bin-averaged vertical turning wavelengths (large dots) are 250 ± 20 sm, consistent with the vortex-trapped wave model (solid curve) and an order of magnitude larger than the time-dependent Ekman layer model (dotted curve). To reproduce a vertical wavelength of 250 sm, the Ekman model would require an eddy viscosity of $1000 \times 10^{-4} \text{ m}^2 \text{ s}^{-1}$, corresponding to a viscous decay time k_z^2/V_e of only 4 h. For vorticities of $-0.35f$ to $-0.1f$, the observed turning wavelengths remain at ~ 250 sm while both models predict smaller values. For vorticities of $-0.1f$ to 0.0 , a vortex-trapped wave cannot exist and the observed λ_z bears some resemblance to a time-dependent Ekman layer (dotted curve). However, we note that there are only a few scattered data points and little clockwise-in-time kinetic energy associated with the diurnal signal (Fig. 14a) at these vorticities. This reflects the tendency for weak diurnal signals to accompany weak vorticities due to fortnightly modulation of both signals in sync with the fortnightly beating of the barotropic O_1 and K_1 diurnal tides.

Vertical wavenumber spectra from 100-900 sm (50-800 m) depth shown in Fig. 15 affirm the rotary character of the signal with depth. The shear layer over the summit plain appears as a peak at a vertical wavelength $\lambda_z = 256$ sm in the $r = 0-3$ km counterclockwise-with-depth (CCW) spectrum, most pronounced in the variance-preserving spectrum. There is no corresponding enhancement in the clockwise-with-depth (CW) spectrum at this wavelength. The CW spectrum is redder ($k_z^{-5/2}$) than the GM model (Garrett and Munk 1975; Cairns and Williams 1976) but has comparable levels for $\lambda_z > 50$ sm. At radii greater than 10 km, there are no significant peaks in either the CCW or CW spectra. Both have the same spectral slope but slightly lower (0.7GM) levels. Spectral slopes are steeper (k_z^{-3}) for vertical wavelengths $\lambda_z < 50$ sm.

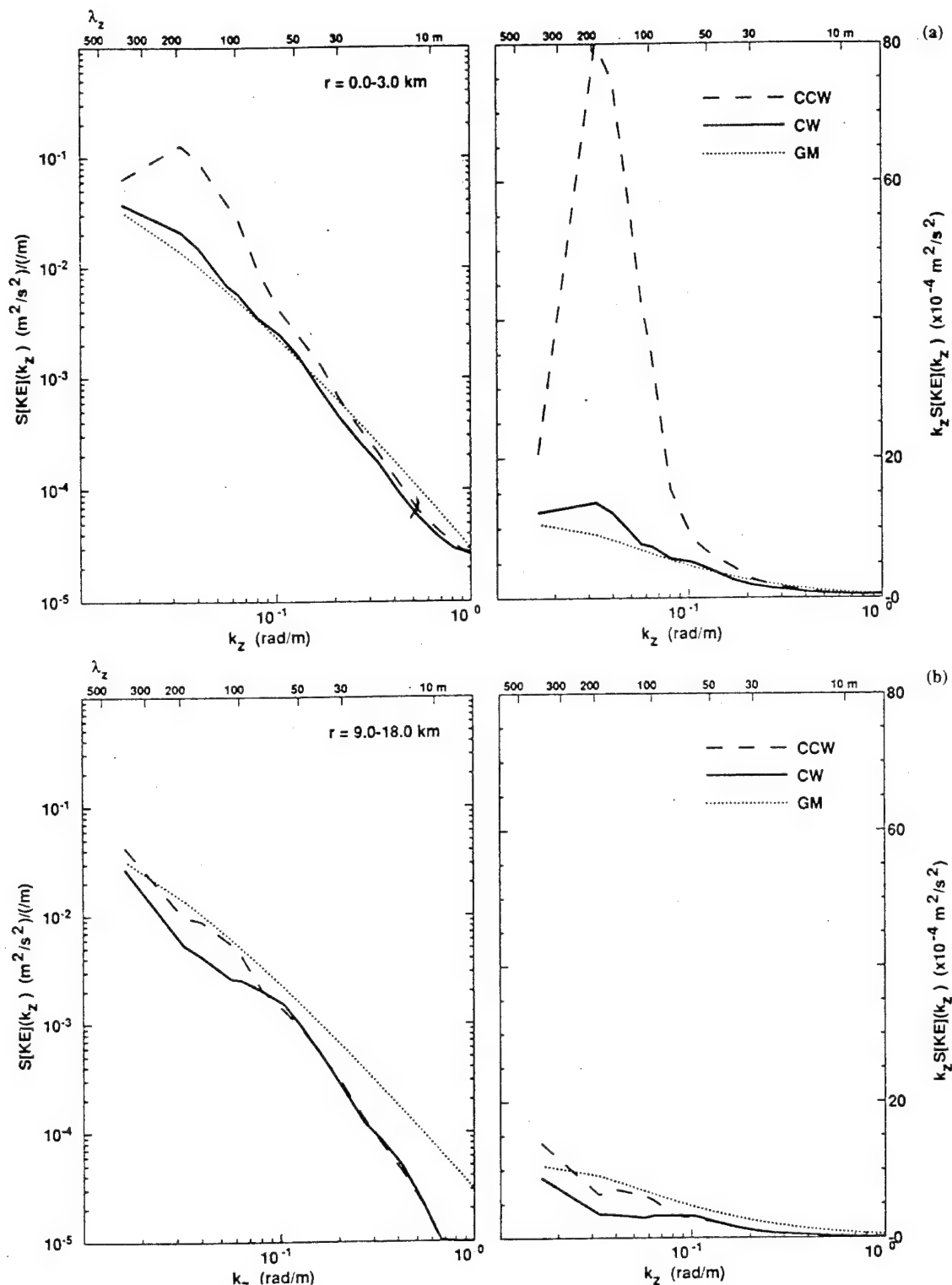


Figure 15: Vertical wavenumber spectra of rotary kinetic energy from 100-900 sm (50-800 m depth) for drops at 0-3 km (upper two panels) and 9-12 km radius (lower two panels). Spectra are presented in both log-log (left panels) and variance-preserving (right panels) formats. The dotted curves correspond to the GM model spectrum. The 0-3 km spectra emphasize the depth-rotary nature of the shear-layer signal above the summit plain. They are dominated by a counterclockwise-with-depth (CCW) peak at $\lambda_z = 256$ sm. There is no corresponding enhancement of CW energy. Away from the seamount, clockwise and counterclockwise spectra are similar and slightly below GM levels.

Figure 16 compares the horizontal structure of the amplitude and phase for the $\lambda_z = 256$ -sm CCW component with that for gravest seamount- or vortex-trapped modes. The observed structure resembles the gravest mode in that the largest vectors are found above the summit plain and exhibit nearly uniform orientation. Moving off the summit plain, the observed vectors become weaker and of more random orientation. Comparing just the radial decay of amplitude, Fig. 17 displays an envelope of solutions for the vortex-trapped near-inertial wave model constrained by the observed buoyancy frequency N , vortex radius r_0 , vorticity ζ , and vertical wavelength λ_z (gray stippling); model amplitude has been normalized by the value at $r = 0$. Further constraining the Eulerian frequency to be equal to the K_1 diurnal frequency produces the black envelope of solutions. Both seamount- and vortex-trapped wave models, and the XCP data (\bullet), show the largest signal inside the vortex and radial decay on scales of a few kilometers outside the vortex. Since the gravest-mode horizontal structure for the two wave models is nearly identical, it cannot be used to distinguish which model is more appropriate.

5.3 Radial heat-flux

A striking feature in the summit plain current-meter records is the radial heat-flux $\langle u_r' T' \rangle$ associated with the diurnal oscillations (Brink 1995a; Eriksen 1995b). Johnson and Sanford (1980) reported similar correlations between vertical displacements and outward velocities on the flanks of Bermuda which they interpreted as evidence of an anisotropic internal wave field. Radial velocity/vertical displacement correlations are also seen in the profiler data on the Fieberling summit plain. Vertical wavenumber coherences $\langle u_r' v_\theta' \rangle$, $\langle u_r' \xi' \rangle$ and $\langle v_\theta' \xi' \rangle$ are significant at vertical wavelengths $\lambda_z = 100$ -300 sm for $r = 6$ -10 km (Fig. 18). At these wavelengths, u_r' and v_θ' are 90° out of phase, consistent with the counterclockwise turning with depth of the horizontal velocity vector (Fig. 12). Radial velocity u_r' and vertical displacement $\xi' = -T'/\bar{T}_z$ are roughly 180° out of phase, implying an outward radial heat-flux. It follows that azimuthal velocity v_θ' and vertical displacement ξ' are 90° out of phase. These properties are more consistent with a vortex-trapped near-inertial

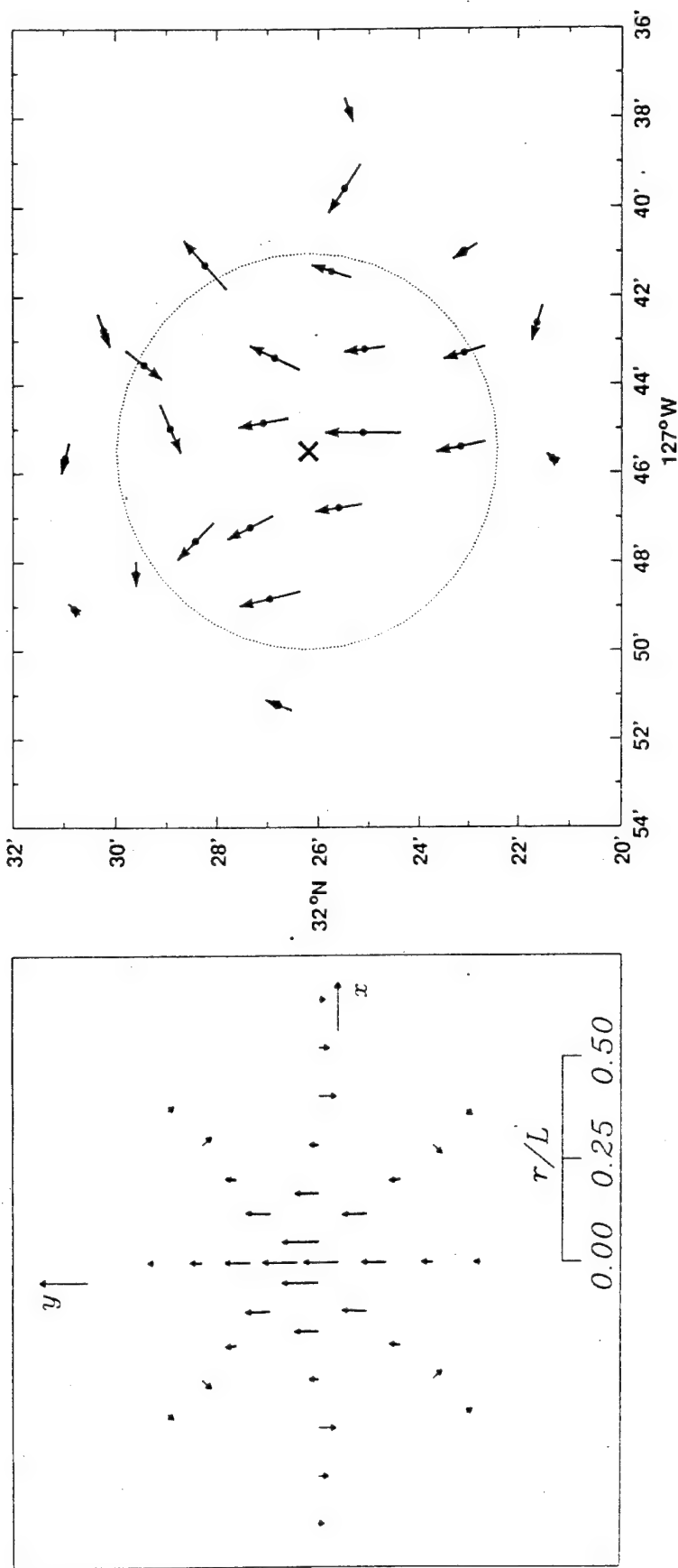


Figure 16: Horizontal structure for gravest seamount- or vortex-trapped modes (left panel; after Brink, 1989) compared to the amplitude and phase of the observed $\lambda_z = 256$ -m counterclockwise-with-depth signal (right panel). The seamount- and vortex-trapped wave have identical horizontal structure. The observations have been averaged in $2' \times 2'$ bins. Over the summit plain, the signal is strongest and has nearly uniform orientation. Off the summit, amplitudes are weaker and the orientation more random.

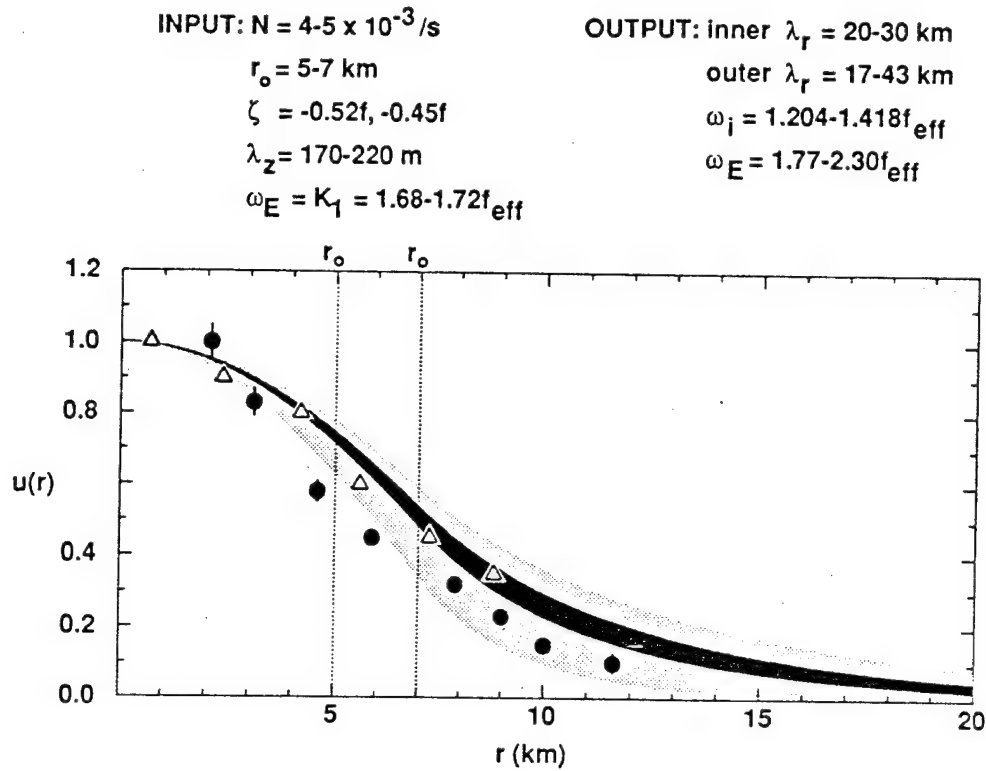


Figure 17: Radial structure of horizontal velocity for a vortex-trapped mode (stippled envelope) constrained by the observed range of buoyancy frequency N , core vorticity ζ , core radius r_o and vertical wavelength λ_z . If further constrained to have the observed K_1 diurnal Eulerian frequency, the solid envelope results, corresponding to an inner radial wavelength of 27 km and an outer (decay) radial wavelength $\lambda_{r_o} = 25$ km. A seamount-trapped wave has identical radial structure (\blacktriangle). XCP observations (\blacklozenge) lie near the model curves.

FIEBERLING XCP/HRP

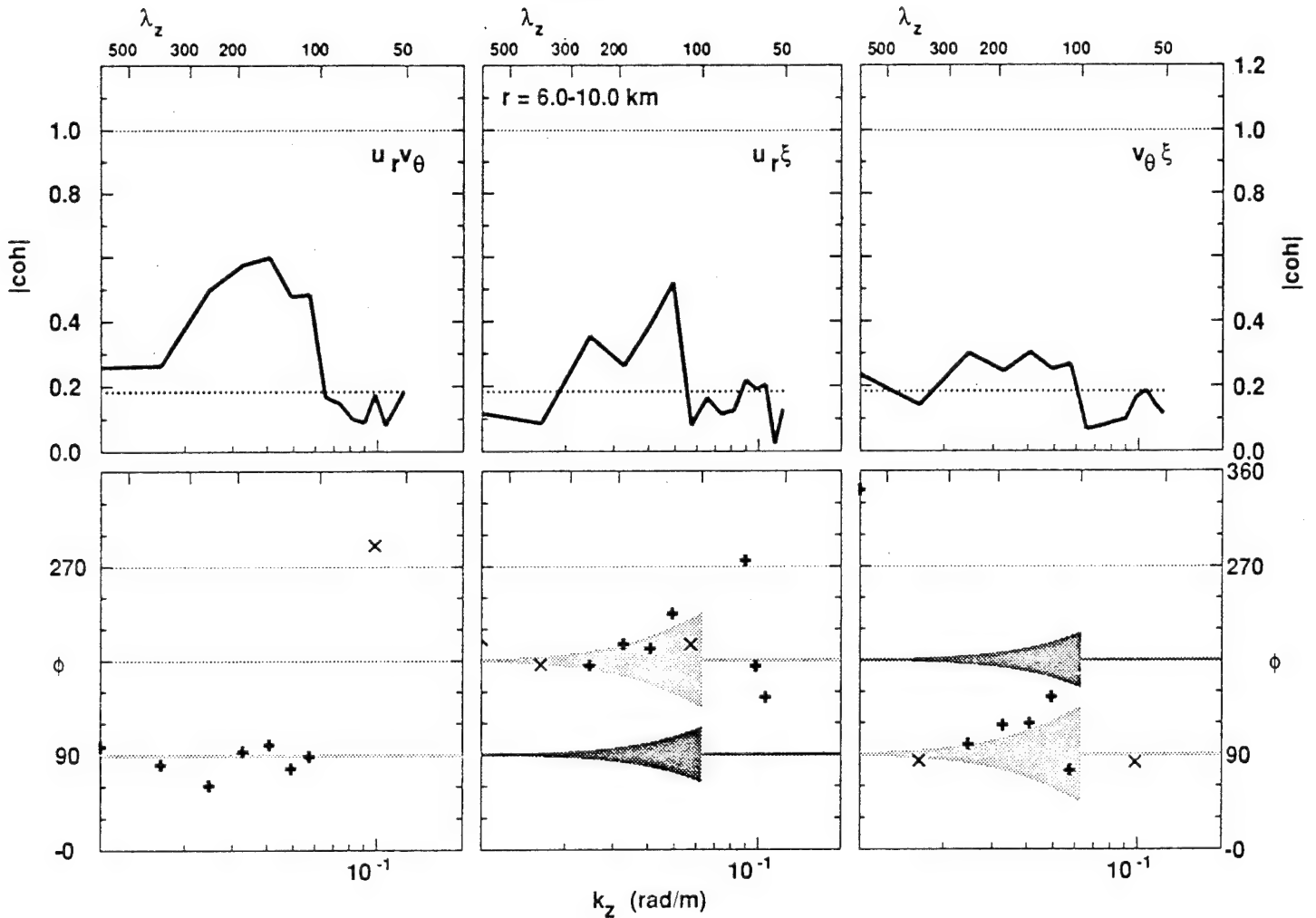


Figure 18: Coherence magnitude (upper panels) and phase (lower panels) as functions of vertical wavenumber for $r = 6-10$ km. Phase is only plotted where the coherence is significant (+) or coherence between east and north velocity components is significant (x). Phase relations for vortex- and seamount-trapped waves are shown by the light and dark stippling, respectively. Spreading of the phase relations by eddy diffusivities or viscosities K_e and $V_e \leq 10 \times 10^{-4} \text{ m}^2 \text{ s}^{-1}$ (Appendices A and B) is shown for $\lambda_z > 100$ m. Coherence is significant for vertical wavelengths of 100-300 m. In this band, radial and azimuthal velocities are 90° out of phase (consistent with the CCW turning with depth), radial velocity u_r' and vertical displacement ξ' are 180° out of phase (corresponding to an outward radial heat-flux), and azimuthal velocity v_θ' and vertical displacement ξ' are 90° out of phase. These last two phase relations are consistent with vortex-trapped but not seamount-trapped waves.

internal wave than a seamount-trapped topographic wave. Adding turbulent damping with K_p and $V_e \leq 10 \times 10^{-4} \text{ m}^2 \text{ s}^{-1}$, consistent with the observed turbulence levels, causes the theoretical phase relations to diverge from their inviscid values (Appendices A and B), but not by enough to explain the data with seamount-trapped fluctuations (Fig. 12).

The radial structure of the radial displacement-flux $\langle u_r \xi' \rangle$, shown in Fig. 19 (solid curve), resembles that of a vortex-trapped wave (dashed), having a zero crossing near 3-km radius, positive values inside that radius and negative values outside. We caution that Haidvogel *et al.* (1993) found a radial heat-flux in numerical simulations where the forcing frequency and Coriolis frequency f were too far apart for a vortex-trapped wave to exist. They made no mention of an azimuthal heat-flux.

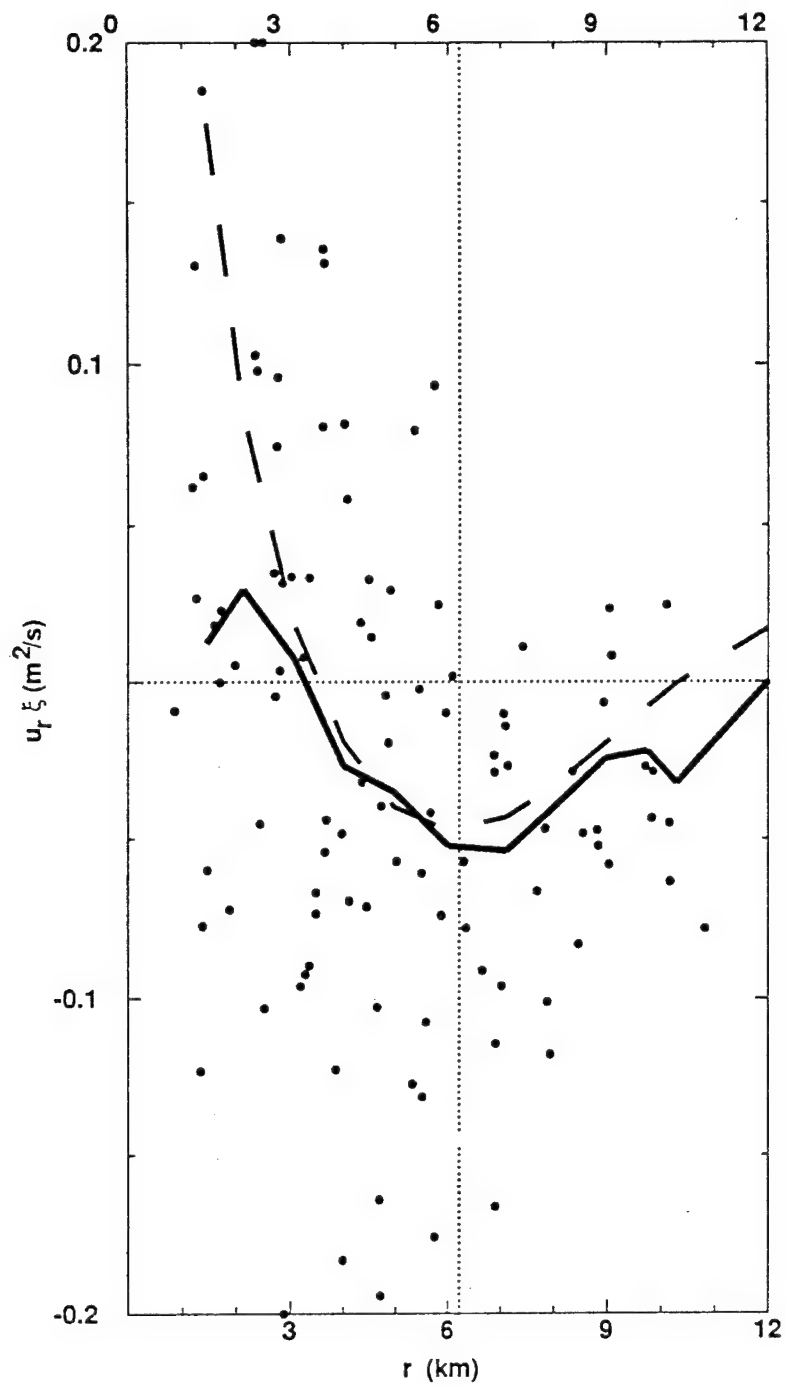


Figure 19: Radial structure of the real (co-spectral) part of the radial displacement flux $u_r \tilde{\xi}'$ in the $\lambda_z = 100\text{-}300$ m band. Dots and triangles correspond to values from individual XCPs and HRPs, respectively. Solid curves are radial bin averages. The dashed curve depicts a vortex-trapped wave model prediction.

6. FINESCALE INSTABILITY, TURBULENCE AND MIXING

Commensurate with the large amplitude and small vertical scale of the diurnal velocity signal above the seamount summit, the finescale gradient Richardson number $Ri = N^2/V_z^2$ associated with these motions was frequently ≤ 0.25 (Fig. 20). The cumulative probability distribution for 10-m Ri above the summit contrasts markedly with that from profiles 10 km away (Fig. 21). In the far field, only 3% of the 10-m Ri samples are less than 0.25, while 21% of the summit 10-m Ri values lie below 0.25. Also, 3% of the summit samples contain 10-m density inversions (10-m $N^2 < 0$, corresponding to 10-m $Ri < 0$ in Fig. 21) while no overturns are found on this scale in the far field. Low Ri above the summit plain is controlled principally by the diurnal shear. The shear of the mean vortex was relatively small and incapable of supporting near-critical Richardson numbers on its own. However, its contribution to the total shear is not inconsequential; the superposition of mean and diurnal shears modulates Ri temporally and azimuthally. Temporal variability in Ri is evident in the HRP time-series as depth-bands of low Ri propagating downward with the phase speed of the diurnal velocity signals. At times, this results in layers of $Ri < 0.25$ well above the bottom as in Fig. 20.

Stability theory (Miles and Howard 1961) and laboratory studies (Thorpe 1978) suggest that flow at low gradient Richardson number ($Ri < 0.25$) is susceptible to shear instabilities. Finescale density profiles above the summit reveal frequent inversions suggestive of the vertical overturning that characterizes this process (Fig. 20). The histogram of Thorpe (1977) overturn scales over the summit, where the average buoyancy frequency is $4.5 \times 10^{-3} \text{ s}^{-1}$, reveals a significant number of Thorpe overturns thicker than 4 m (Fig. 22). No turbulent patches with overturning scales of this size were found at comparable depths away from the seamount. Nabatov and Ozmidov (1988) report similarly large overturns atop Ampere and Josephine Seamounts in the North Atlantic.

Associated with the low- Ri values and thick vertical overturns in the 200-m thick diurnal shear layer above the summit plain were intense turbulence signals (Fig. 20). Assuming 3-D isotropy as appropriate for

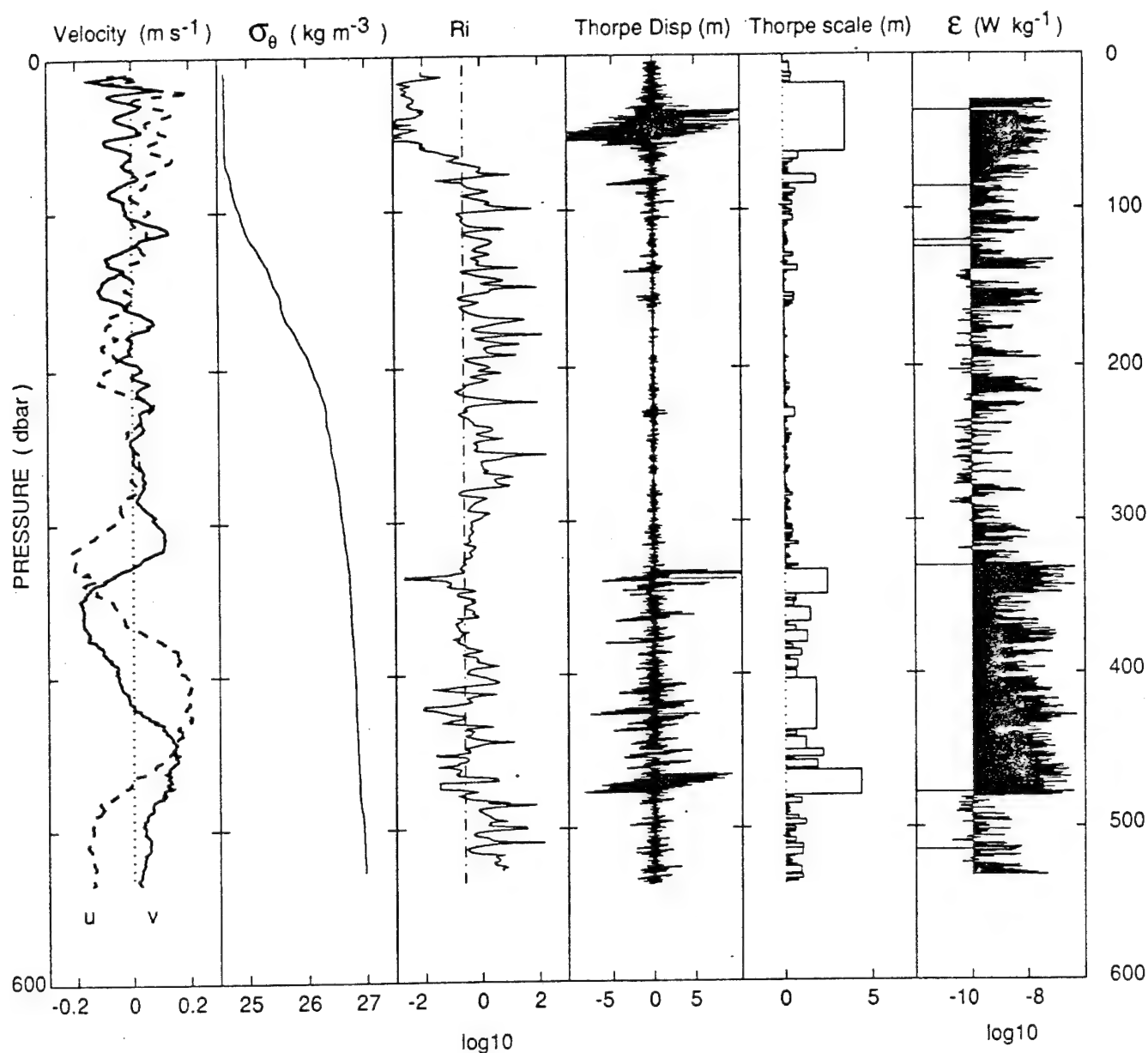


Figure 20: A representative HRP profile from the center of the Fieberling Guyot summit plain. Panels include profiles of east and north velocity, u and v , with the depth-averaged velocities removed, potential density σ_θ , 10-m linear least-squares-fit Richardson number $Ri = N^2/(u_z^2 + v_z^2)$, Thorpe displacements and Thorpe scales for each overturning patch (defined as the interval over which the sum of Thorpe displacements is zero), and turbulent kinetic energy dissipation rate ϵ averaged in 0.5-m bins. The elevated velocity signals below 300-m depth are accompanied by more frequent occurrences of $Ri < 0.25$, larger Thorpe displacements and scales, and higher turbulent dissipation rates ϵ .

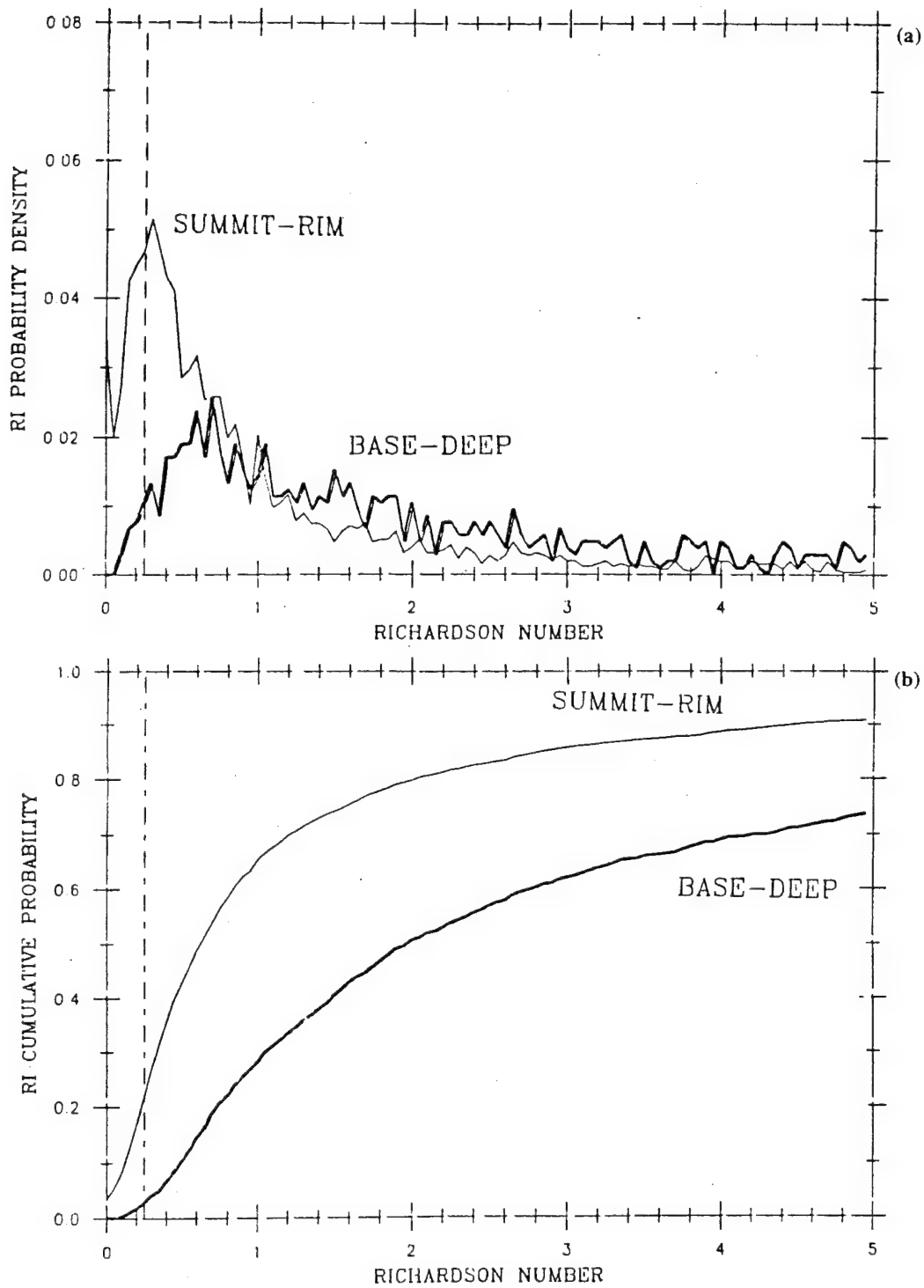


Figure 21: The (a) probability and (b) cumulative probability density distributions of 10-m Ri over the summit plain (thick) and 10-km away from the seamount (thin). The broken line demarks $Ri = 0.25$.

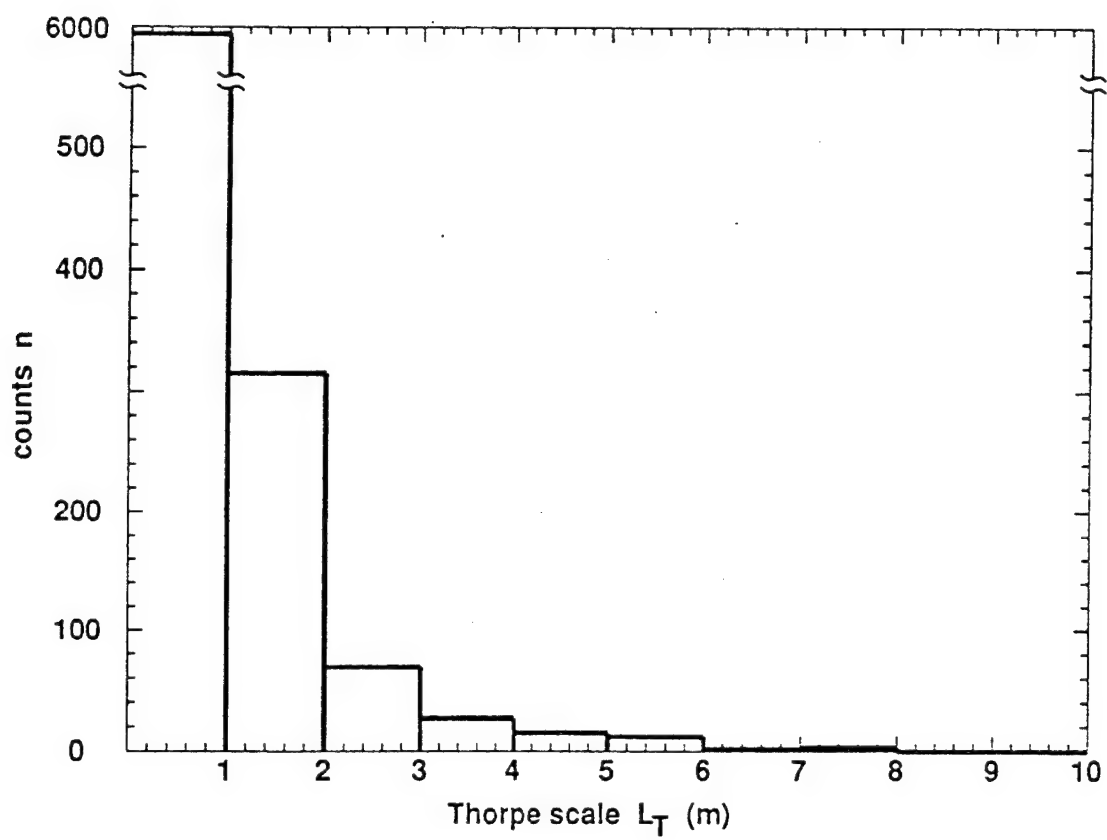


Figure 22: Histogram of Thorpe scales above the summit plain.

turbulent Reynolds numbers $\epsilon/(vN^2) > 200$ (Gargett *et al.* 1984), instantaneous kinetic energy dissipation rates exceed $\epsilon = 10^{-6} \text{ W kg}^{-1}$ (Fig. 20) and temperature variance dissipation rates exceed $\chi_T = 10^{-7} \text{ C}^2 \text{ s}^{-1}$ within the turbulent patches. Nabatov and Ozmidov (1988) similarly reported 10-m thick patches of turbulence above and in detached layers in the vicinity of Ampere and Josephine Seamounts with turbulent dissipation rates of $(0.6-40) \times 10^{-6} \text{ W kg}^{-1}$.

Instantaneous dissipation rates of comparable magnitude were also found in the upper 100 m of the water column near Fieberling Guyot both in the surface mixed-layer during periods of strong wind-stress (ϵ) and in the strongly stratified pycnocline immediately below it (ϵ and χ_T) (Fig. 20). The signals just below the base of the mixed layer are associated with the upper-ocean internal wave field and exhibit no systematic spatial variation with respect to the seamount. In contrast, between 300- and 700-m depth, the turbulent dissipation rate in the 150-m thick diurnal shear layer above the summit plain is consistently 10-100 times larger than that at similar depths 10 km away (Fig. 23a).

The vertically-averaged kinetic energy dissipation rate below 300-m depth above the summit plain (based on profiles at or inside the summit rim) is $(3.3 \pm 0.1) \times 10^{-8} \text{ W kg}^{-1}$. One measure of the significance of this dissipation rate is the time it would take it to quench energies of the diurnal oscillation and vortex cap. These have average total energy densities of $\sim 5 \times 10^{-3} \text{ m}^2 \text{ s}^{-2}$ and $2.5 \times 10^{-3} \text{ m}^2 \text{ s}^{-2}$, respectively, comprised mostly of kinetic energy. Assuming these flows are the energy source for the turbulence, the observed average dissipation rate would drain the diurnal oscillation and vortex in about three days. By comparison, it takes open-ocean turbulence 100 days to deplete a canonical Garrett-Munk internal wave field (Garrett 1979). Barotropic tides must be supplying energy at a rate comparable to the dissipation rate to maintain the observed signals. This further explains the spring-neap fluctuations in both the strength of the vortex cap (Fig. 6) and diurnal shear; this strongly dissipative system is incapable of ringing for any appreciable time. Irreversible turbulent

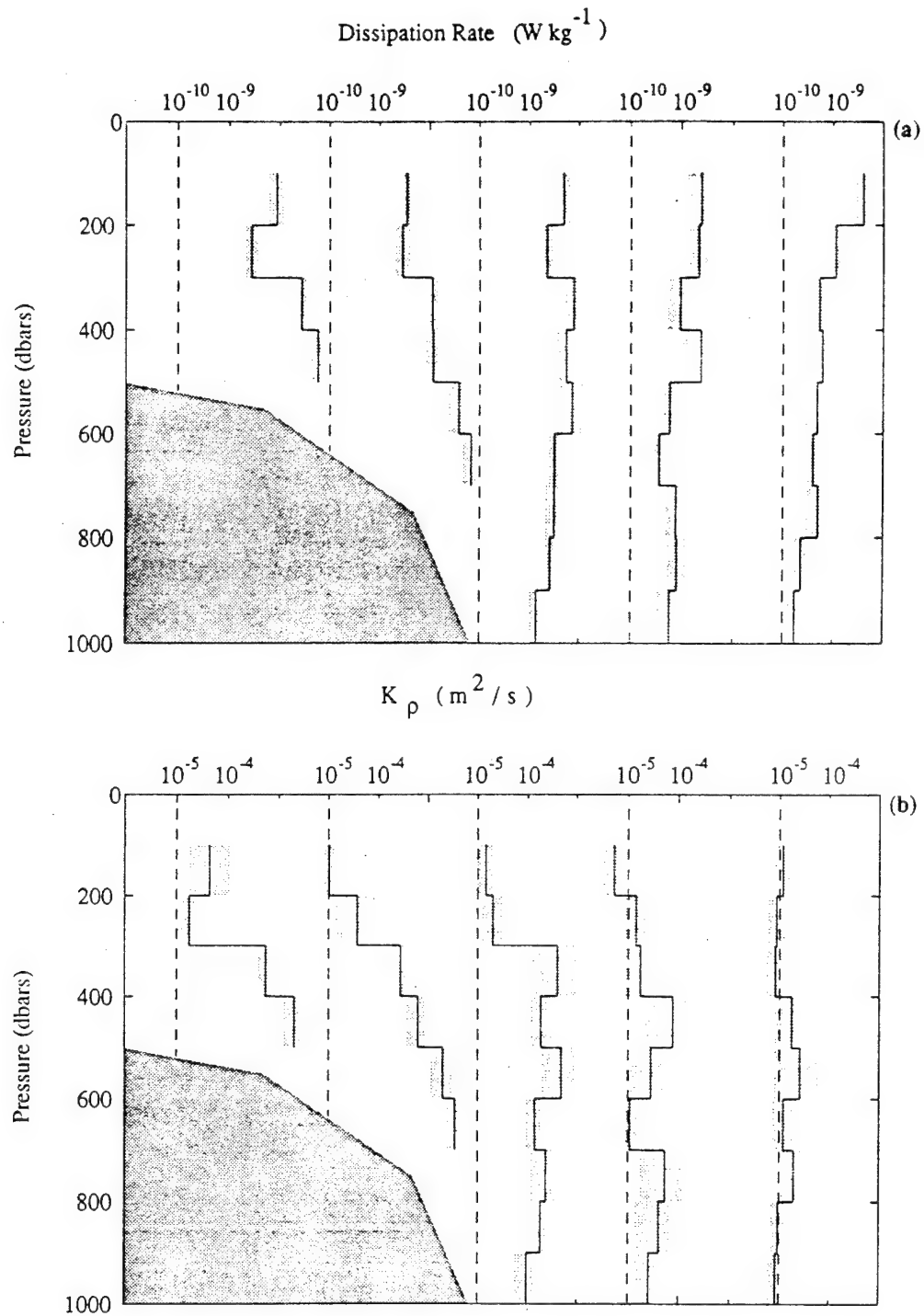


Figure 23: Average kinetic energy dissipation rates ϵ (a) and diapycnal eddy diffusivities K_ρ (b) as a function of depth and radial distance from the seamount. The 0.5-m ϵ estimates are averaged into 100-m thick vertical bins and lateral bins grouped (i) above the summit plain, (ii) at the summit rim, (iii) about the 1500-m isobath, (iv) about the 2500-m isobath, and (v) more than 10 km from the seamount. Lateral spacing of the average profiles is not to scale and the topography is schematic. The bracketing 95% uncertainties were computed with a bootstrap technique (Efron and Gong 1983; Polzin 1992) and do not differ substantially from those computed assuming a log-normal distribution (Baker and Gibson 1987). Eddy diffusivities (b) were inferred from the kinetic energy dissipation rates following Osborn (1980) using a mixing efficiency of 0.25 (Oskey 1982). Error bounds in (b) are 95% confidence limits from (a).

processes clearly play a major role in the flow dynamics above Fieberling Guyot.

Mirroring the radial patterns in dissipation rate ϵ , the average diapycnal eddy diffusivities inferred from the microstructure data increase by two orders of magnitude approaching the seamount summit (Fig. 23b). Background diffusivities of $\sim 0.1 \times 10^{-4} \text{ m}^2 \text{ s}^{-1}$, as typical of the open-ocean pycnocline (Gregg 1989; Polzin *et al.* 1995), were observed 10 km away from the guyot. The inferred eddy diffusivity, averaged over the volume inside the summit rim between 300-m depth and the bottom, is $(30 \pm 20) \times 10^{-4} \text{ m}^2 \text{ s}^{-1}$, corresponding to a vertical buoyancy-flux of $O(10^{-8} \text{ m}^2 \text{ s}^{-3})$. Lueck and Mudge (1996) report a comparable average diffusivity above Cobb Seamount at 47°N , 170 km north of Fieberling Guyot. Excluding depths shallower than 300 m, where thermohaline interleaving is evident and might enhance χ_T estimates, roughly consistent diffusivities are estimated from temperature variance dissipation rates [$K_T = \chi_T / (2\bar{T}_z^2)$, Osborn and Cox 1972] and kinetic energy dissipation rates ($K_p \leq \gamma \epsilon / \bar{N}^2$, Osborn 1980) using a mixing efficiency $\gamma = 0.25$ (Oakey 1982).

The layer of intensified turbulence above the summit plain extends well into the stratified water column so the concern that near-bottom turbulence might contribute little mixing because it acts on already well-mixed water (Garrett 1990) is not germane here. For reference, the height scale for a steady Ekman layer is only 8 m for an effective eddy viscosity of $50 \times 10^{-4} \text{ m}^2 \text{ s}^{-1}$ (assuming a turbulent Prandtl number of one). At greater depths, Toole *et al.* (1996) and Eriksen (1995a) infer eddy diffusivities of $(2.0\text{--}6.0) \times 10^{-4} \text{ m}^2 \text{ s}^{-1}$ in the stratified boundary layer above the flanks of Fieberling. There, the source of energy for the turbulent mixing appears to be high-frequency internal waves critically-reflected from the sloping sides of the seamount.

7. SUMMARY AND DISCUSSION

Fine- and microstructure profiles collected over Fieberling Seamount reveal a 200-m thick layer of intensified activity overlying the summit plain. In this layer co-exists (i) an anticyclonic vortex cap of relative vorticity $-0.5f$ (Fig. 2b), (ii) $O(N)$ subinertial diurnal shear (Figs. 9 and 10), and (iii) elevated turbulence with average kinetic energy dissipation rates $\epsilon = (3.3 \pm 0.1) \times 10^{-8} \text{ W kg}^{-1}$ (Fig. 23a) and microstructure-inferred eddy diffusivities of $K_p = (30 \pm 20) \times 10^{-4} \text{ m}^2 \text{ s}^{-1}$ (Fig. 23b). All these motions appear to be driven, at least in part, by the barotropic K_1 and O_1 diurnal tides. The turbulent dissipation rate implies a decay time of about three days for the diurnal oscillation and vortex, so barotropic tides must be continually pumping energy into the summit motions to maintain them.

7.1 Vortex

The vortex was roughly in cyclogeostrophic balance inside $r = 4 \text{ km}$ (Fig. 8). At larger radii and depths greater than 600 m, the observed radial pressure gradient and effective Coriolis acceleration do not balance. This imbalance cannot be explained by contributions from momentum-flux divergences and appears to be an artifact of inadequate azimuthal sampling. Beckmann and Haidvogel (1996) find the vortex cap in their simulations to be in near balance.

The vortex cap appears to be maintained by both (i) squashing of impinging background flow and (ii) tidal rectification. The vortex strength changes dramatically every few months (Fig. 6) depending on the direction of the impinging background flow (Brink 1995), suggestive of Taylor-Proudman effects. The impinging flow would have to renew water over the summit plain every three days to maintain a Taylor cap against turbulent dissipation. This requires impinging flows strong enough to cross the summit in less than 3 days time, or flows of at least 3 cm s^{-1} while impinging flows are generally about 2 cm s^{-1} (Brink 1995).

Evidence for vortex maintenance by tidal rectification includes (i) the short turbulent decay time, (ii) vortex strength exhibiting a fortnightly cycle of $\pm 0.3f$ (Fig. 6), and (iii) the vortex core containing a *negative* potential vorticity anomaly (Fig. 7). Recent work by Codiga (1996) indicates that forcing at the bottom and dissipation within the water column leads to rectification in the right sense to produce an anticyclonic vortex for seamount-trapped waves. Beckmann and Haidvogel (1996) suggest that vortex-trapped waves will lift an existing vortex up off the bottom. The strong role of rectification at Fieberling raises doubts about past interpretations of observed isopycnal doming over seamounts in terms of Taylor-Proudman dynamics.

Brink (1995) argued that the outward radial heat-flux could be maintaining the vortex cap's dome of cold water over the summit against benthic Ekman downwelling $\bar{w}\bar{T}_z$ [$\bar{w} = (-0.08 \pm 0.05) \text{ cm s}^{-1}$ as he inferred from observed near-bottom radial outflow of $\bar{u}_r = 1\text{--}2 \text{ cm s}^{-1}$, $\bar{T}_z = 10^{-2} \text{ }^\circ\text{C m}^{-1}$]. Current-meter radial heat-fluxes are $\langle u_r T \rangle = 0.4^\circ\text{C cm s}^{-1}$ (Brink 1995; Eriksen 1995b), an order of magnitude higher than the fluxes found here (Fig. 19) though the profiler surveys took place during a neap and do not include barotropic velocities.

There are subtleties in the rectification problem which frustrate inferring balances from incomplete data. Consider steady ($\partial/\partial t = 0$), azimuthally-averaged ($\partial/\partial\theta = 0$) conservation of azimuthal momentum and buoyancy within a vortex

$$\boxed{(f + \zeta)\bar{u}_r} = -\frac{\partial\langle u_r'v_\theta' \rangle}{\partial r} - \frac{2\langle u_r'v_\theta' \rangle}{r} - \boxed{\frac{\partial\langle v_\theta'w' \rangle}{\partial z}} - V_e \frac{\partial^2 V_\theta}{\partial z^2} \quad (5)$$

6 0 0 20 $1 \times 10^{-7} \text{ m s}^{-2}$

$$\bar{u}_r \frac{\partial \bar{B}}{\partial r} + \boxed{\bar{N}^2 \bar{w}} = -\boxed{\frac{1}{r} \frac{\partial [r \langle u_r' b' \rangle]}{\partial r}} - \frac{\partial K_p}{\partial z} \bar{N}^2 \quad (6)$$

0.2 2 2 1 $\times 10^{-9} \text{ m s}^{-3}$

$$\boxed{\frac{1}{r} \frac{\partial(r\tilde{u}_r)}{\partial r} + \frac{\partial\tilde{w}}{\partial z} = 0}, \quad (7)$$

$\times 10^{-7} \text{ s}^{-1}$

where $\zeta = V_\theta/r + \partial V_\theta/\partial r$ is the background mean vorticity, b' , u_r' , v_θ' and w' are the wave buoyancy, radial, azimuthal and vertical velocities, and \tilde{u}_r and \tilde{w} are the *wave-induced mean* cross-stream circulation. Values are deduced from Table 1. Note that the fortnightly acceleration of the vortex azimuthal velocity is $\partial V_\theta/\partial t = 5 \times 10^{-7} \text{ m s}^{-2}$ while the fortnightly rate of change of the vortex buoyancy anomaly is $\partial \bar{B}/\partial t = 4 \times 10^{-12} \text{ m s}^{-3}$. Eriksen's (1995b) estimate of $\langle v_\theta' w' \rangle$ assumes a balance between time rate of change and vertical advection. From (5), it seems to be a factor of 2-4 too high even taking into account acceleration of the vortex. Substituting (5) and (6) into continuity (7) and, recognizing that the constants of integration are zero for a spatially-confined wave field, we find that the steady balance reduces to

$$\frac{\langle v_\theta' w' \rangle}{f + \zeta} = -\frac{\langle u_r' b' \rangle}{\bar{N}^2} = \langle u_r' \xi' \rangle \quad (8)$$

$\times 10^{-1} \text{ m}^2 \text{ s}^{-1}$

where the imbalance can be accounted for by the factor of 2-4 overestimate of $\langle v_\theta' w' \rangle$. This relation holds exactly for inviscid unforced vortex-trapped waves. That is, wave fluxes exactly balance wave-induced mean advective fluxes to maintain a steady state; the background field remains unchanged by the waves' flux-divergences unless irreversible forcing or dissipation break interrelationship (8). This is a general result for waves propagating in a background mean shear known as the *nonacceleration theorem* (Andrews and McIntyre 1976; Dunkerton 1980). Thus, with only partial measurements of the flux divergences, the net impact of the forcing, fluctuations and dissipation on the background cannot be evaluated.

Hopes of quantifying wave-induced mean accelerations from numerical models where dissipative processes are prescribed using unverified parameterizations are likewise frustrated. Beckmann and Haidvogel's (1996) Fieberling simulation is relatively insensitive to the

TABLE 1

Quantities for the azimuthally-averaged equations (5-7).

<i>variables</i>	<i>value</i>	<i>source</i>
f	$8 \times 10^{-5} \text{ s}^{-1}$	
$f + \zeta$	$4 \times 10^{-5} \text{ s}^{-1}$	
\bar{N}^2	$2 \times 10^{-5} \text{ s}^{-2}$	
\bar{T}_z	$10^{-2} \text{ }^\circ\text{C m}^{-1}$	
$H = \frac{\lambda_z}{2\pi}$	50 m	(Fig. 14)
L	5 km	
ξ_0	4 m	(Fig. 7)
$\bar{B} = \bar{N}^2 \xi_0$	$-8 \times 10^{-5} \text{ m s}^{-2}$	
$K_\rho = \frac{\langle w'b' \rangle}{\bar{N}^2}$	$3 \times 10^{-3} \text{ m}^2 \text{ s}^{-1}$	(Fig. 23)
\bar{u}_r	$1.5 \times 10^{-2} \text{ m s}^{-1}$	(Brink 1995)
\bar{w}	$-8 \times 10^{-4} \text{ m s}^{-1}$	(Brink 1995)
$\langle u_r'v_\theta' \rangle$	0	(Fig. 18)
$\langle v_\theta'b' \rangle$	0	(Fig. 18)
$\langle u_r'b' \rangle$	$10^{-7} \text{ m}^2 \text{ s}^{-3}$	(Brink 1995; Eriksen 1995b)
	$0.1 \times 10^{-7} \text{ m}^2 \text{ s}^{-2}$	(Fig. 19)
$\langle v_\theta'w' \rangle$	$10^{-4} \text{ m}^2 \text{ s}^{-2}$	(Fig. 7 of Eriksen 1995b)

magnitude of bottom friction and epineutral diffusivities, but comparable isosigma mixing produced damping times of 300 seconds. They find a balance between $\bar{u}_r \partial \bar{B} / \partial r$ and $\bar{N}^2 \bar{w}$ in contrast to the numbers in (6), and radial heat-fluxes in the opposite sense to the observations, that is, acting to remove the cold dome (baroclinic instability). Without knowing the detailed nature and spatial distribution of the forcing and dissipative processes in models, or measuring all the flux-divergences in the field, the net rate of change of background dynamic quantities cannot be determined unambiguously.

7.2 Diurnal shear

The diurnal shear above the summit plain also displays a fortnightly modulation of K_1 beating against O_1 (Noble *et al.* 1994; Brink 1995). Its jet-like horizontal structure rotates clockwise with time and counterclockwise with depth ($\lambda_z = 250$ sm). Its slightly subinertial frequency (Fig. 9) and azimuthal-mode-one horizontal structure (Figs. 16 and 17) closely resemble those of a seamount-trapped topographic wave (Brink 1989; 1990). However, vortex-trapped near-inertial internal waves share these properties (Kunze *et al.* 1995). The (i) continuous counterclockwise turning of the velocity vector with depth (Figs. 12 and 13), (ii) nonzero radial heat-flux, and (iii) near-zero azimuthal heat-flux (Figs. 18 and 19) more closely resemble a vortex-trapped internal wave than either free or forced seamount-trapped topographic waves. The heat-fluxes are the most convincing argument in favor of a vortex-trapped wave interpretation as subinertial benthic Ekman layers also exhibit counterclockwise turning with depth albeit with smaller scales (Fig. 14).

We conclude that the layer of intense diurnal shear observed in the HRP and XCP measurements atop the summit plain is best-described as a vortex-trapped near-inertial internal wave, its subinertial frequency allowed by the strong negative vorticity of the vortex cap. With its frequency determined by diurnal tidal forcing and its horizontal scale controlled by the vortex size, the vertical wavelength of a vortex-trapped wave is set by the wave dispersion relation (2).

The inviscid vortex-trapped wave model (Kunze *et al.* 1995) predicts vertical and horizontal structure for tidally-generated diurnal motions consistent with the observations, but it does not predict amplitude. The Richardson number and microstructure observations suggest that turbulent dissipation driven by shear instability limit the magnitude of the diurnal oscillations. Energy supplied by the barotropic tide impinging on the seamount will raise the amplitude of the vortex-trapped wave until unstable Froude number $|V_z|/N$ is achieved. Subsequent energy will be dissipated by shear-driven turbulence to sustain a sufficiently unstable $|V_z|/N$ to account for the dissipation (Kunze *et al.* 1990). Thus, equilibrium vortex and diurnal amplitudes will be established such that the energy being supplied by the barotropic tide is lost to turbulent dissipation at the same rate. This equilibrium will be set up on a timescale of a few days since the dissipation timescale is three days; vortex and diurnal strengths track the spring-neap cycle of the barotropic tide with no discernible lag. For Fieberling Guyot's $\bar{N} = 4.5 \times 10^{-3} \text{ rad s}^{-1}$ and a vertical wavelength $\lambda_z = 210 \text{ m}$, a Froude number $|V_z|/N = 2.0$ corresponds to velocities of 30 cm s^{-1} which are achieved when the diurnal and vortex shear are additive.

How then do we account for the evanescent diurnal signal found over the flanks that is coherent with motions above the summit plain (Eriksen 1995b). Vortex-trapped waves cannot exist on the flanks so these must be bottom-trapped motions. This is consistent with the flank azimuthal heat-flux dominating over the radial heat-flux (Eriksen's Fig. 7). He models them as forced evanescent oscillations, that is, off-resonant forced topographic waves. The downslope phase propagation he observed then implies upslope energy propagation. This upslope energy-flux must be accumulating and dissipating on the summit. We speculate that it feeds energy into the summit vortex-trapped motions.

Vortex-trapped internal waves forced by diurnal tides should be found only just poleward of 30° . Equatorward of 30° , diurnal frequencies can propagate as free internal waves so will not be trapped. Poleward of 43° , a vortex cap could not be strong enough to allow a finite-scale free diurnal

wave within its confines (Fig. 24). This is consistent with Codiga's (1996) interpretation of the diurnal signal in repeated ADCP surveys over Cobb Seamount (46°45'N) as a seamount-trapped wave. Thus, while intensified baroclinic tidal oscillations appear to be a common feature of seamount summits, their dynamics appears to be a strong function of latitude.

Vorticity-trapped diurnal waves are also likely to arise along the continental shelf break. Tidal rectification will drive poleward flow on the eastern boundary and equatorward flow on the western boundary. Negative vorticity associated with these currents will trap subinertial internal waves driven by diurnal tides for latitudes ~30°-40°, by semidiurnal tides for latitudes greater than 70° and by annual tides near the equator. The cross-slope heat-flux $\langle u'T' \rangle$ and vertical momentum-flux $\langle v'w' \rangle$ associated with these trapped oscillations may redistribute or drive stronger along-slope currents, such as the California Undercurrent (Hickey 1979).

7.3 Turbulent mixing

Elevated turbulence levels of $\epsilon \gtrsim 10^{-7} \text{ W kg}^{-1}$ are found coincident with the vortex cap and diurnal oscillation, corresponding to eddy diffusivities of $O(10 \times 10^{-4} \text{ m}^2 \text{ s}^{-1})$. Geometric scaling arguments provide a means of assessing the local and global importance of seamount mixing (Lueck and Mudge 1996). Applying their approach to Fieberling, the layer of intensified turbulence atop the seamount has a horizontal area of $A_s \sim 100 \text{ km}^2$. Therefore, the average inferred diffusivity on the summit implies a diapycnal buoyancy-flux of $F_b = K_\rho A_s N^2 \simeq (25 \times 10^{-4} \text{ m}^2 \text{ s}^{-1}) \times (10^8 \text{ m}^2) \times (10^{-5} \text{ s}^{-2}) = 2.5 \text{ m}^4 \text{ s}^{-3}$. Substantial evidence has accumulated in recent years to support an interior (i.e., away from boundaries) diapycnal diffusivity $\sim 0.1 \times 10^{-4} \text{ m}^2 \text{ s}^{-1}$ (Moum and Osborn 1986; Gregg 1989; Ledwell *et al.* 1993; Toole *et al.* 1994; Polzin *et al.* 1995). Thus, the interior ocean area required to support the same diapycnal buoyancy-flux found over the seamount summit is $2.5 \times 10^4 \text{ km}^2$, or 250 times the area of the summit plain mixing zone.

Applying the same arguments on the basin scale, consider a density surface that intersects the intense mixing layer atop the seamount. Ignoring

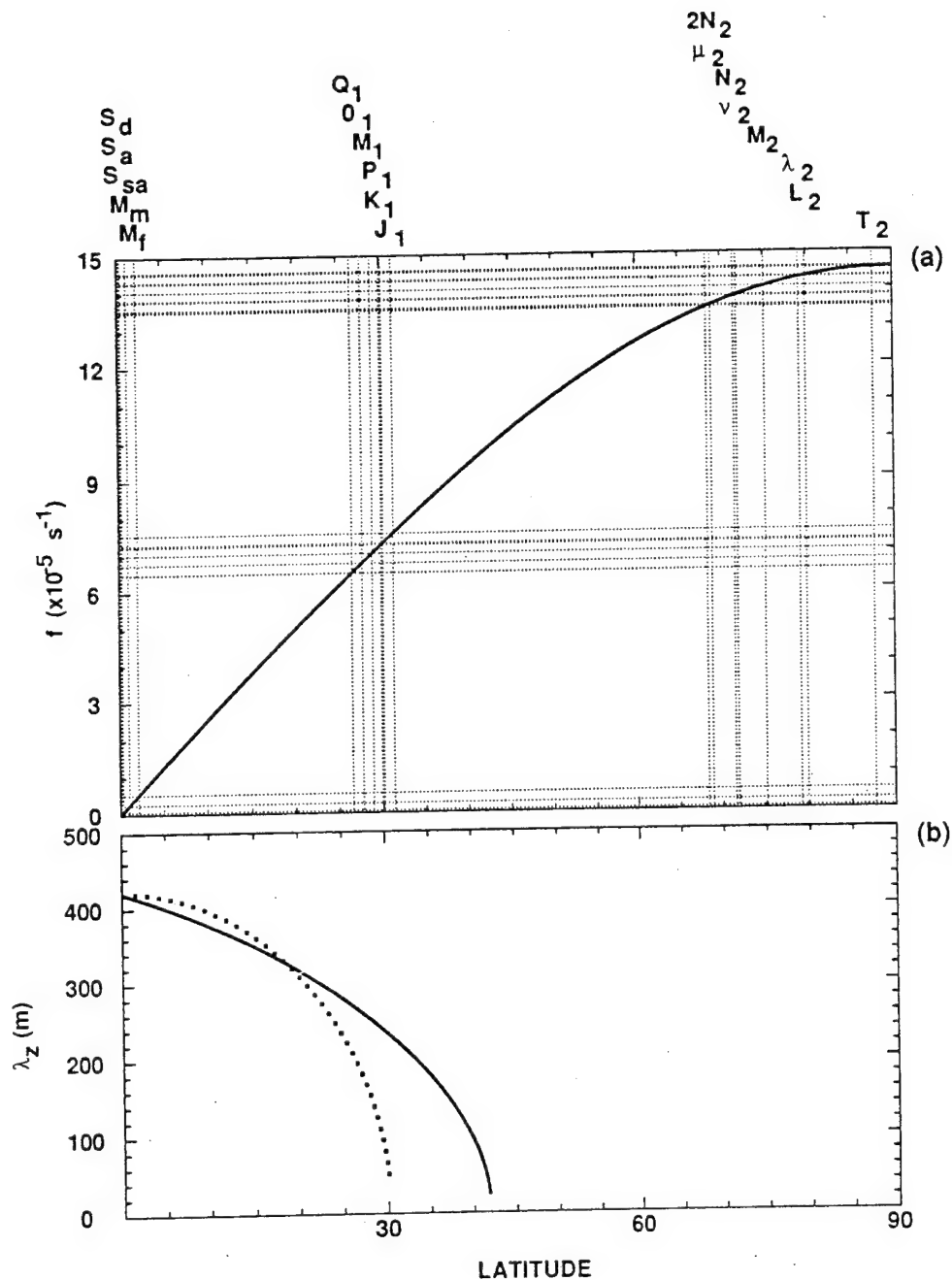


Figure 24: (a) Intersects of the tidal constituent frequencies (Neumann and Pierson, 1966) and the Coriolis frequency f as a function of latitude. Decadal through fortnightly tides cluster within 2° of the equator, diurnal tides straddle 30° and semidiurnal tides resonate at latitudes greater than 68° . (b) The vertical wavelength λ_z of a K_1 Eulerian frequency internal wave with horizontal wavelength 30 km. The dotted curve corresponds to a quiescent ocean where free diurnal-frequency internal waves are not possible poleward of 30° . The solid curve corresponds to a vortex of core relative vorticity $-0.5f$ and azimuthal mode $n = -1$ for which diurnal internal waves can exist equatorward of 42° .

that this surface may outcrop farther north, its surface area north of 20°N in the Pacific is about $3.8 \times 10^7 \text{ km}^2$. Hypsometric data reveals that 0.014 of this surface lies within 300 m (the thickness of the intensely turbulent layer above Fieberling's summit plain) of the ocean bottom (see Fig. 7 of Toole *et al.* 1996). For summit \bar{N}^2 values, we deduce a diffusive diapycnal buoyancy-flux for the *interior* N. Pacific pycnocline of $(3.8 \times 10^{13} \text{ m}^2) \times (0.1 \times 10^{-4} \text{ m}^2 \text{ s}^{-1}) \times (10^{-5} \text{ s}^{-2}) = 4 \times 10^3 \text{ m}^4 \text{ s}^{-3}$. If we assume that the average diffusivity in the majority of the near-boundary regions is comparable to that observed above the summit plain, the corresponding near-boundary buoyancy-flux is $(0.014) \times (3.8 \times 10^{13} \text{ m}^2) \times (25 \times 10^{-4} \text{ m}^2 \text{ s}^{-1}) \times (10^{-5} \text{ s}^{-2}) = 13 \times 10^3 \text{ m}^4 \text{ s}^{-3}$, three times larger than the interior buoyancy-flux. The total (interior plus near-boundary) inferred buoyancy-flux is about half what would be obtained with a spatially-uniform diapycnal diffusivity of $10^{-4} \text{ m}^2 \text{ s}^{-1}$ acting over the whole surface. However, only a small fraction of the near-boundary region is occupied by seamount summits. Continental slopes and flanks of midocean ridges and seamounts account for most of the near-boundary area. Toole *et al.* (1996) and Eriksen (1995a) estimate effective diffusivities of $(2-6) \times 10^{-4} \text{ m}^2 \text{ s}^{-1}$ for the stratified turbulent boundary layer adjacent to the flanks of Fieberling. Taking this diffusivity as more representative of the near-bottom average reduces the near-boundary buoyancy-flux to $(1-3) \times 10^3 \text{ m}^4 \text{ s}^{-3}$, comparable to the interior flux. Under this assumption, the interior plus near-boundary buoyancy-flux falls to $\sim 6 \times 10^3 \text{ m}^4 \text{ s}^{-3}$, only 15% of what would result from a spatially-uniform diapycnal diffusivity of $10^{-4} \text{ m}^2 \text{ s}^{-1}$.

From the above arguments, we conclude that, on a local scale, seamounts like Fieberling Guyot constitute very significant sites for diapycnal exchange as also found by Lueck and Mudge (1996). However, on basin scales, there does not appear to be sufficient ocean area in close proximity to seamount summits to support average diapycnal transports equivalent to those that would be associated with the canonical (Munk 1966) $10^{-4} \text{ m}^2 \text{ s}^{-1}$ diffusivity in the main pycnocline. Ideal thermocline theory (e.g., Luyten *et al.* 1983) demonstrates that diapycnal transports of this magnitude are not necessary in the main pycnocline.

In contrast, direct mass and heat budgets for abyssal basins (e.g., Hogg *et al.* 1982; Roemmich *et al.* 1995) *do* require average diapycnal diffusivities of $O(10^{-4} \text{ m}^2 \text{ s}^{-1})$. As Toole *et al.* (1996) discuss, the characteristic hypsometry of deep ocean basins results in abyssal density surfaces having a large fraction of their area in close proximity to the bottom (their Fig. 7). The average diffusivity on a given density surface is obtained by weighting the high diffusivities near topography by the fraction of the ocean basin proximal to bathymetry on that surface,

$$K_p = \frac{K_s \cdot A_s}{A_{tot}} + \frac{K_i \cdot (A_{tot} - A_s)}{A_{tot}} \approx K_i + \frac{K_s \cdot A_s}{A_{tot}}. \quad (9)$$

Taking near-boundary diffusivities K_s comparable to those found atop the summit plain, waters below 3000-m depth will have average diapycnal diffusivity raised above $10^{-4} \text{ m}^2 \text{ s}^{-1}$ while, for near-boundary diffusivities close to observed flank values, depths below 4500 m will have average diffusivities exceeding $10^{-4} \text{ m}^2 \text{ s}^{-1}$ due to near-boundary mixing. Thus, while topographically-induced mixing plays at most a comparable role to weak interior mixing in the main pycnocline, it could dominate near the ocean bottom to drive $O(10^{-4} \text{ m}^2 \text{ s}^{-1})$ abyssal diffusivities.

Acknowledgments: We thank Charlie Eriksen and Ken Brink for making their moored current-meter data available. Valuable insights into seamount-trapped waves and tidal rectification arose from discussions with Ken Brink, Dan Codiga and Aike Beckmann. The HRP data were collected and analysed under ONR contract N00014-89-J-1073. The XCP data were collected under ONR contract N00014-90-J-1535 and analyzed under contracts N00014-90-J-1535 and N00014-94-I-0038.

APPENDIX A: VISCOUS NEAR-INERTIAL WAVES

Consider the equations of motion for hydrostatic rectilinear internal waves of the form $\Psi = \Psi_0(r) \cdot \exp[i(k_x x + k_z z - \omega_i t)]$, where $\mathbf{k} = (k_x, 0, k_z)$ is the wavevector chosen so the horizontal direction of propagation lies along the x -axis ($k_y = 0$) and ω_i the intrinsic frequency damped by eddy viscosity V_e and eddy diffusivity K_e ,

$$-i\omega_i u - fv = -ik_x p + V_e k_z^2 u$$

$$-i\omega_i v + fu = V_e k_z^2 v$$

$$0 = -ik_z p + b \quad \Rightarrow \quad \boxed{p = \frac{-i b}{k_z}} \quad (\text{A1})$$

$$-i\omega_i b + N^2 w = K_e k_z^2 b \quad \Rightarrow \quad \boxed{b = \frac{-i N^2 w}{(\omega_i - i K_e k_z^2)}}$$

$$k_x u + k_z w = 0 \quad \Rightarrow \quad \boxed{w = \frac{-k_x u}{k_z}}$$

so that

$$[\omega_i - i V_e k_z^2] \cdot u - fv = \frac{N^2 k_x^2 \cdot u}{(\omega_i - i K_e k_z^2) k_z^2} \quad (\text{A2})$$

$$-[i\omega_i + V_e k_z^2] \cdot v + fu = 0 \quad \Rightarrow \quad \boxed{v = \frac{-ifu}{(\omega_i - i V_e k_z^2)}}$$

and the buoyancy can be expressed in terms of the zonal velocity u as

$$b = \frac{iN^2k_x u}{(\omega_i - iK_e k_z^2)k_z} \quad (A3)$$

Substituting the boxed expression for v in (A2) into the first expression in (A2) and assuming weakly-damped ($V_e k_z^2, K_e k_z^2 \ll f$) near-inertial ($N^2 k_x^2 \ll f^2 k_z^2$) waves, the dispersion relation can be approximated by

$$\omega_i + i\sigma = f + \frac{N^2 k_x^2}{2f k_z^2} + iV_e k_z^2 \quad (A4)$$

The effect of viscosity appears as a weak evanescence σ in time (or in the direction of energy propagation C_g). Within the context of this approximation, the eddy diffusivity has no impact on the dispersion relation because near-inertial waves have relatively weak buoyancy signals. More general viscous internal wave behavior can be found in LeBlond (1966). For $V_e = 10 \times 10^{-4} \text{ m}^2 \text{ s}^{-1}$ and $\lambda_z = 100\text{-}300 \text{ m}$, $V_e k_z^2 = (0.4\text{-}4.0) \times 10^{-6} \text{ s}^{-1}$ so is much smaller than the Coriolis frequency $f = 7.8 \times 10^{-5} \text{ s}^{-1}$. Substituting dispersion relation (A4) into (A3) and (A2), we obtain the following consistency relations between the buoyancy b , north velocity v , and east velocity u

$$b = \frac{N^2 k_x}{f k_z} \left[i - i \frac{N^2 k_x^2}{2f^2 k_z^2} + \frac{(V_e - K_e)k_z^2}{f} \right] \cdot u \quad (A5)$$

$$v = -i \left[1 - \frac{N^2 k_x^2}{2f^2 k_z^2} \right] \cdot u.$$

The phase relations between uv , ub and vb are then

$$\phi_{uv} = \frac{\pi}{2}$$

$$\phi_{ub} = \text{Arctan} \left[\frac{2f^2 k_z^2 - N^2 k_x^2}{2f k_z^2 (V_e - K_e) k_z^2} \right] \approx \text{Arctan} \left[\frac{f}{(V_e - K_e) k_z^2} \right] \quad (A6)$$

$$\phi_{vb} = \text{Arctan}\left[\frac{-(V_e - K_e)k_z^2}{f}\right],$$

so that the two horizontal velocity components remain 90° out of phase but the velocity and buoyancy perturbations have slightly modified phase relations if the eddy viscosity and diffusivity differ from zero *and* each other (eddy Prandtl number $V_e/K_e \neq 1.0$). For eddy viscosities and diffusivities $V_e, K_e \leq 10 \times 10^{-4} \text{ m}^2 \text{ s}^{-1}$ and $\lambda_z = 100 \text{ m}$, the phase relations differ by at most 3° from their inviscid values (Fig. 18).

APPENDIX B: VISCOUS STRATIFIED TOPOGRAPHIC WAVES

Following Rhines (1970) and Appendix A, the equations of motion rotated in the vertical plane to lie parallel to topography for plane stratified bottom-trapped topographic waves with eddy viscous V_e and diffusive K_e forcing on gentle slopes ($\alpha \ll 1$) are

$$\begin{aligned} -i(\omega - iV_e k_{\perp}^2)u_{\parallel} - fv &= -ik_{\parallel}p + b\alpha \\ -i(\omega - iV_e k_{\perp}^2)v + fu_{\parallel} &= -ik_y p \\ f\alpha v &= -ik_{\perp}p + b \end{aligned} \tag{B1}$$

$$-i(\omega - iK_e k_{\perp}^2)b = -N^2\alpha u_{\parallel} \quad \Rightarrow \quad b = \frac{-iN^2\alpha u_{\parallel}}{(\omega - iK_e k_{\perp}^2)}$$

$$k_{\parallel}u_{\parallel} + k_y v = 0 \quad \Rightarrow \quad v = \frac{-k_{\parallel}u_{\parallel}}{k_y},$$

where (u_{\parallel}, v) are the across- and along-isobath velocities parallel to the bottom, the flow normal to the bottom w_{\perp} is assumed to vanish identically, and $(k_{\parallel}, k_y, k_{\perp})$ are the across-isobath, along-isobath and normal wavenumbers in a coordinate system lying in the plane of the bathymetry. It has been assumed that $k_{\perp} \gg k_{\parallel}, k_y$ in the viscous terms, consistent with the observations. Substituting the boxed expressions for buoyancy b and along-isobath velocity v into the first three expressions of (B1),

$$\begin{aligned} \left[\frac{-i(\omega - iV_e k_{\perp}^2)}{k_{\parallel}} + \frac{f}{k_y} + \frac{iN^2\alpha^2}{(\omega - iK_e k_{\perp}^2)k_{\parallel}} \right] u_{\parallel} &= -ip \\ \left[\frac{i(\omega - iV_e k_{\perp}^2)k_{\parallel}}{k_y^2} + \frac{f}{k_y} \right] u_{\parallel} &= -ip \end{aligned} \tag{B2}$$

$$\left[\frac{-f\alpha k_{\parallel}}{k_y k_{\perp}} + \frac{iN^2\alpha}{(\omega - i\mathbf{K}_e k_{\perp}^2)k_{\perp}} \right] u_{\parallel} = -ip$$

or, equating the lefthand sides,

$$(\omega - i\mathbf{V}_e k_{\perp}^2)(\omega - i\mathbf{K}_e k_{\perp}^2) = \frac{N^2\alpha^2 k_y^2}{k_H^2} \quad (\text{B3})$$

$$(\omega - i\mathbf{V}_e k_{\perp}^2)(\omega - i\mathbf{K}_e k_{\perp}^2)k_{\parallel}k_{\perp} - ifk_y k_{\perp}(\omega - i\mathbf{K}_e k_{\perp}^2) - N^2\alpha k_y^2 = 0.$$

which can be solved for ω and k_{\perp} in terms of $N, f, \alpha, \mathbf{V}_e, \mathbf{K}_e, k_y$ and k_{\parallel} .

Assuming that the frequency ω is altered only slightly so that it can be expressed as a small perturbation from the inviscid solution

$\omega = N\alpha k_y/k_H + \delta\omega$, where $\delta\omega \ll N\alpha k_y/k_H$, the first equation in (B3) implies

$$\omega \approx \frac{N\alpha k_y}{k_H} + \frac{i(\mathbf{V}_e + \mathbf{K}_e)k_{\perp}^2}{2} \quad (\text{B4})$$

where $N\alpha k_y/k_H \approx f \gg \mathbf{V}_e k_{\perp}^2, \mathbf{K}_e k_{\perp}^2$ from before. Substituting (B4) into the second equation in (B3) gives

$$\frac{N^2\alpha^2 k_y k_{\parallel} k_{\perp}}{k_H^2} - ifk_{\perp} \left(\frac{N\alpha k_y}{k_H} + \frac{i(\mathbf{V}_e - \mathbf{K}_e)k_{\perp}^2}{2} \right) - N^2\alpha k_y = 0 \quad (\text{B5})$$

and, assuming a solution for k_{\perp} perturbed about the inviscid solution

$$k_{\perp} = \frac{Nk_H^2}{N\alpha k_{\parallel} - ifk_H} = Nk_H^2 \frac{N\alpha k_{\parallel} + ifk_H}{N^2\alpha^2 k_{\parallel}^2 + f^2 k_H^2}, \quad (\text{B6})$$

leads to a viscous perturbation

$$\delta k_{\perp} = \frac{N^2 f (\mathbf{V}_e - \mathbf{K}_e) k_H^8}{2\alpha k_y (N\alpha k_{\parallel} - ifk_H)^4}. \quad (\text{B7})$$

This could blow up if $k_y = 0$, invalidating the small perturbation approximation. Based on the observational results of a diurnal Eulerian frequency $\omega_E = K_1$ and an imaginary vertical wavenumber at most comparable to the real vertical wavenumber, $k_z \simeq \text{Re}\{k_\perp\}$, we can quantify the relationship between buoyancy b and u_\parallel in (B1)

$$b \simeq \frac{-iN^2\alpha u_\parallel}{f + \frac{i(V_e - K_e)k_\perp^2}{2}} \simeq \frac{-N^2\alpha}{f} \left[\frac{(V_e - K_e)k_z^2}{2f} + i \right] u_\parallel, \quad (\text{B8})$$

independent of the direction of across-slope propagation, so the phase relation between u_\parallel and b becomes

$$\phi_{ub} = \text{Arctan}\left(\frac{2f}{(V_e - K_e)k_z^2}\right) \quad (\text{B9})$$

for topographic waves that are either propagating and standing across slope. The phase relation between u_\parallel and b is perturbed from the inviscid solution by half the amount that viscous near-inertial waves are perturbed from their inviscid solution. We apply viscous phase relation offsets (A6) and (B9) to seamount- and vortex-trapped waves under the assumption that seamount axisymmetric geometry is not a major consideration.

REFERENCES

- Andrews, D.G., and M.E. McIntyre, 1976: Planetary waves in horizontal and vertical shear: The generalized Eliassen-Palm relation and the mean zonal acceleration. *J. Atmos. Sci.*, **33**, 2049-2053.
- Baines, P., 1971: The reflection of internal/inertial waves from bumpy surfaces. Part 1. *J. Fluid Mech.*, **46**, 273-291.
- Baker, M.A., and C.H. Gibson, 1987: Sampling turbulence in the stratified ocean: Statistical consequences of strong intermittency. *J. Phys. Oceanogr.*, **17**, 1817-1836.
- Beckmann, A., and D.B. Haidvogel, 1996: A numerical simulation of flow at Fieberling Guyot. submitted to *J. Geophys. Res.*
- Bell, T.H., 1975: Topographically-generated internal waves in the open ocean. *J. Geophys. Res.*, **80**, 320-327.
- Boyer, D.L., and X. Zhang, 1990: Motion of oscillatory currents past isolated topography. *J. Phys. Oceanogr.*, **20**, 1425-1448.
- Brink, K.H., 1989: The effect of stratification on seamount-trapped waves. *Deep-Sea Res.*, **36**, 825-844.
- Brink, K.H., 1990: On the generation of seamount-trapped waves. *Deep-Sea Res.*, **37**, 1569-1582.
- Brink, K.H., 1995a: Tidal and lower frequency currents above Fieberling Guyot. *J. Geophys. Res.*, **100**, 10,817-10,832.
- Brink, K.H., 1995b: On the nonlinear bottom Ekman layer. *J. Geophys. Res.*, submitted.
- Cairns, J.L., and G.O. Williams, 1976: Internal wave observations from a midwater float, 2. *J. Geophys. Res.*, **81**, 1943-1950.
- Chapman, D.C., 1989: Enhanced subinertial diurnal tides over isolated topographic features. *Deep-Sea Res.*, **36**, 815-824.
- Chapman, D.C., and D.B. Haidvogel, 1992: Formation of Taylor caps over a tall isolated seamount in a stratified ocean. *Geophys. Astrophys. Fluid Dyn.*, **64**, 31-65.
- Codiga, D.L., 1991: Fitting Fieberling Guyot. *TopoNews*, Newsletter of ONR Accelerated Research Initiative Flow Over Abrupt Topography, **4**, 14-15.
- Codiga, D.L., 1993: Laboratory realizations of stratified seamount-trapped waves. *J. Phys. Oceanogr.*, **23**, 2053-2071.
- Codiga, D.L., 1996: Observations and physics of amplified subinertial tidal currents in stratification and mean shear flow at a seamount. *Ph.D. thesis*, U of Washington, 92 pp.
- Dunkerton, T.J., 1980: A Lagrangian-mean theory of wave/mean flow interaction with applications to nonacceleration and its breakdown. *Rev. Geophys. Space Phys.*, **18**, 387-400.

- Efron, B., and G. Gong, 1983: A leisurely look at the bootstrap, the jackknife and cross-validation. *Amer. Stat.*, **37**, 36-48.
- Eriksen, C.C., 1982: Observations of internal wave reflection off sloping bottoms. *J. Geophys. Res.*, **87**, 525-538.
- Eriksen, C.C., 1985: Implications of ocean bottom reflection for internal wave spectra and mixing. *J. Phys. Oceanogr.*, **15**, 1145-1156.
- Eriksen, C.C., 1991: Observations of amplified flows atop a large seamount. *J. Geophys. Res.*, **96**, 15,227-15,236.
- Eriksen, C.C., 1995a: Internal wave reflection and mixing at Fieberling Guyot. *J. Geophys. Res.*, submitted.
- Eriksen, C.C., 1995b: Waves, mean flows and mixing at a seamount. *Topographic Effects in the Ocean, Proceedings 'Aha Huliko'a Hawaiian Winter Workshop*, P. Müller and D. Henderson, Eds., U of Hawaii, Honolulu, HI, 1-13. .
- Flierl, G.R., and R.P. Mied, 1985: Frictionally-induced circulations and spindown of a warm-core ring. *J. Geophys. Res.*, **90**, 8917-8927.
- Freeland, H., 1994: Ocean circulation at and near Cobb Seamount. *Deep-Sea Res.*, **41**, 1715-1732.
- Gargett, A.E., T.R. Osborn and P.W. Nasmyth, 1984: Local isotropy and the decay of turbulence in a stratified fluid. *J. Fluid. Mech.*, **144**, 231-280.
- Garrett, C., 1979: Mixing in the ocean interior. *Dyn. Atmos. Oceans*, **3**, 239-265.
- Garrett, C., 1990: The role of secondary circulation in boundary mixing. *J. Geophys. Res.*, **95**, 989-993.
- Garrett, C.J.R., and W.H. Munk, 1975: Space-time scales of internal waves: A progress report. *J. Geophys. Res.*, **80**, 291-297.
- Genin, A., P.K. Dayton, P.F. Lonsdale and F.N. Spiess, 1986: Corals on seamount peaks provide evidence of current acceleration over deep-sea topography. *Nature*, **322**, 59-61.
- Genin, A., M. Noble and P.F. Lonsdale, 1989: Tidal currents and anticyclonic motions on two North Pacific seamounts. *Deep-Sea Res.*, **36**, 1803-1815.
- Genin, A., C.K. Paull and W.P. Dillon, 1992: Anomalous abundances of deep-sea fauna on a rocky bottom exposed to strong currents. *Deep-Sea Res.*, **39**, 293-302.
- Gilbert, D., and C. Garrett, 1989: Implications for ocean mixing of internal wave scattering off irregular topography. *J. Phys. Oceanogr.*, **19**, 1716-1729.
- Gregg, M.C., 1989: Scaling turbulent dissipation in the thermocline. *J. Geophys. Res.*, **94**, 9686-9698.
- Haidvogel, D.B., A. Beckmann, D.C. Chapman and R.-Q. Lin, 1993: Numerical simulation of flow around a tall isolated seamount. Part II: Resonant generation of trapped waves. *J. Phys. Oceanogr.*, **23**, 2373-2391.

- Hickey, B.M., 1979: The California Current system — hypotheses and facts. *Prog. Oceanogr.*, **8**, 191-279.
- Hogg, N.G., 1973: On the stratified Taylor column. *J. Fluid Mech.*, **58**, 517-537.
- Hogg, N.G., P. Biscaye, W. Gardner and W.J. Schmitz, 1982: On the transport and modification of Antarctic Bottom Water in the Vema Channel. *J. Mar. Res.*, **40**(Suppl.), 231-263.
- Hunkins, K., 1986: Anomalous diurnal tidal currents on the Yermak Plateau. *J. Mar. Res.*, **44**, 51-69.
- Huthnance, J.M., 1974: On the diurnal tidal currents over Rockall Bank. *Deep-Sea Res.*, **21**, 23-35.
- Huthnance, J.M., 1978: On coastal-trapped waves: Analysis and numerical calculation by inverse iteration. *J. Phys. Oceanogr.*, **8**, 74-92.
- Johnson, C.L., and T.B. Sanford, 1980: Anomalous behavior of internal gravity waves near Bermuda. *J. Phys. Oceanogr.*, **10**, 2021-2034.
- Kunze, E., 1985: Near-inertial wave propagation in geostrophic shear. *J. Phys. Oceanogr.*, **15**, 544-565.
- Kunze, E., 1986: The mean and near-inertial velocity fields in a warm-core ring. *J. Phys. Oceanogr.*, **16**, 1444-1461.
- Kunze, E., and T.B. Sanford, 1986: Near-inertial wave interactions with mean flow and bottom topography near Caryn Seamount. *J. Phys. Oceanogr.*, **16**, 109-120.
- Kunze, E., M.A. Kennelly and T.B. Sanford, 1992: The depth dependence of shear finestructure off Point Arena and near Pioneer Seamount. *J. Phys. Oceanogr.*, **22**, 29-41.
- Kunze, E., and T.B. Sanford, 1993: Submesoscale dynamics near a seamount. Part I: Measurements of Ertel vorticity. *J. Phys. Oceanogr.*, **23**, 2567-2588.
- Kunze, E., R.W. Schmitt and J.M. Toole, 1995: The energy balance in a warm-core ring's near-inertial critical layer. *J. Phys. Oceanogr.*, **25**, 942-957.
- Kunze, E., A.J. Williams III and M.G. Briscoe, 1990: Observations of shear and vertical stability from a neutrally-buoyant float. *J. Geophys. Res.*, **95**, 18,127-18,142.
- Ledwell, J.R., A.J. Watson and C.S. Law, 1993: Evidence of slow mixing across the pycnocline from an open-ocean tracer-release experiment. *Nature*, **364**, 701-703.
- LeBlond, P.H., 1966: On the damping of internal gravity waves in a continuously-stratified ocean. *J. Fluid Mech.*, **25**, 121-142.
- Levin, L.A., E.L. Leithold, T.F. Gross, C.L. Huggett and C. DiBacco, 1994: Contrasting effects of substrate mobility on infaunal assemblages inhabiting two high-energy settings on Fieberling Guyot. *J. Mar. Res.*, **52**, 489-522.

- Loder, J.H., 1980: Topographic rectification on the sides of Georges Bank. *J. Phys. Oceanogr.*, **10**, 1399-1416.
- Lueck, R.G., and T.D. Mudge, 1996: Topographically-induced mixing around a shallow seamount. *Nature*, submitted.
- Luyten, J.R., J. Pedlosky and H. Stommel, 1983: The ventilated thermocline. *J. Phys. Oceanogr.*, **13**, 292-309.
- Maas, L.R.M., and J.T.F. Zimmerman, 1989a: Tide-topography interactions in a stratified shelf sea. I. Basic equations for quasi-nonlinear internal tides. *Geophys. Astrophys. Fluid Dyn.*, **45**, 1-35.
- Maas, L.R.M., and J.T.F. Zimmerman, 1989b: Tide-topography interactions in a stratified shelf sea. II. Bottom-trapped internal tides and baroclinic residual currents. *Geophys. Astrophys. Fluid Dyn.*, **45**, 37-69.
- McCartney, M., 1975: Inertial Taylor columns on a beta-plane. *J. Fluid Mech.*, **68**, 71-95.
- Miles, J.W., and L.N. Howard, 1961: On the stability of heterogeneous shear flows. *J. Fluid Mech.*, **10**, 496-512.
- Montgomery, E.T., and J.M. Toole, 1993: Fine- and microstructure observations at Fieberling Guyot: R/V New Horizon Cruise Report. Woods Hole Oceanogr. Inst. Tech. Rpt. WHOI-93-15, 27 pp.
- Moum, J.N., and T.R. Osborn, 1986: Mixing in the main thermocline. *J. Phys. Oceanogr.*, **16**, 1250-1259.
- Müller, P., and N. Xu, 1992: Scattering of oceanic internal gravity waves off random bottom topography. *J. Phys. Oceanogr.*, **22**, 474-488.
- Munk, W., 1966: Abyssal recipes. *Deep-Sea Res.*, **13**, 707-730.
- Nabatov, V.N., and R.V. Ozmidov, 1988: Study of turbulence above seamounts in the Atlantic Ocean. *Oceanology*, **28**, 161-166.
- Neumann, G., and W.J. Pierson Jr., 1966: *Principles of Physical Oceanography*. Prentice-Hall Inc., Englewood Cliffs, NJ, 545 pp.
- Noble, M., D.A. Cacchione and W.C. Schwab, 1988: Observations of strong mid-Pacific internal tides above Horizon Guyot. *J. Phys. Oceanogr.*, **18**, 1300-1306.
- Noble, M., and L.S. Mullineaux, 1989: Internal tidal currents over the summit of Cross Seamount. *Deep-Sea Res.*, **36**, 1791-1802.
- Noble, M.A., K.H. Brink and C.C. Eriksen, 1994: Diurnal-period currents trapped above Fieberling Guyot: Observed characteristics and model comparisons. *Deep-Sea Res.*, **41**, 643-658.
- Oakey, N.S., 1982: Determination of the rate of dissipation of turbulent energy from simultaneous temperature and velocity shear microstructure measurements. *J. Phys. Oceanogr.*, **12**, 256-271.
- Osborn, T.R., 1978: Measurements of energy dissipation adjacent to an island. *J. Geophys. Res.*, **83**, 2939-2957.
- Osborn, T.R., 1980: Estimates of the local rate of vertical diffusion from dissipation measurements. *J. Phys. Oceanogr.*, **10**, 83-89.

- Osborn, T.R., and C.S. Cox, 1972: Oceanic finestructure. *Geophys. Fluid Dyn.*, **3**, 321-345.
- Padman, L., A.J. Plueddemann, R.D. Muench and R. Pinkel, 1992: Diurnal tides near the Yermak Plateau. *J. Geophys. Res.*, **97**, 12,639-12,652.
- Phillips, O.M., 1977: *The dynamics of the upper ocean*. Cambridge University Press, Cambridge, 336 pp.
- Polzin, K.L., 1992: Observations of turbulence, internal waves and background flows: An inquiry into the relationships between scales of motion. *Ph.D. thesis*, WHOI Tech. Rpt. 93-39, 244 pp.
- Polzin, K., J.M. Toole and R.W. Schmitt, 1995: Finescale parameterizations of turbulent dissipation. *J. Phys. Oceanogr.*, **25**, 306-328.
- Rhines, P., 1969: Slow oscillations in an ocean of varying depth: Part I. Abrupt topography. *J. Fluid Mech.*, **37**, 161-189.
- Rhines, P., 1970: Edge-, bottom- and Rossby waves in a rotating stratified fluid. *Geophys. Fluid Dyn.*, **1**, 273-302.
- Roden, G.I., 1987: Effect of seamount and seamount chains on ocean circulation and thermohaline structure. *Seamounts, Islands and Atolls*, B.H. Keating, P. Fryer, R. Batiza, and G.W. Boehlert, Eds., AGU, Washington, DC, 335-354.
- Roden, G.I., 1991: Mesoscale flow and thermohaline structure around Fieberling Seamount. *J. Geophys. Res.*, **96**, 16,653-16,672.
- Roden, G.I., 1994: Effects of the Fieberling seamount group upon flow and thermohaline structure in the spring of 1991. *J. Geophys. Res.*, **99**, 9941-9961.
- Roemmich, D., S. Hautala and D. Rudnick, 1995: Northward abyssal transport through the Samoan Passage and adjacent regions. *J. Geophys. Res.*, submitted.
- Sanford, T.B., R.G. Drever, J.H. Dunlap and E.A. D'Asaro, 1982: Design, operation and performance of an expendable temperature and velocity profiler (XTVP). Tech. Rpt. 8110, Appl. Phys. Lab, U of Washington, Seattle, WA 83 pp.
- Sanford, T.B., E.A. D'Asaro, E. Kunze, J.H. Dunlap, R.G. Drever, M.A. Kennelly, M.D. Prater and M.S. Horgan, 1993: An XCP user's guide and reference manual. Tech. Rpt. APL-UW TR 9309, Appl. Phys. Lab, U of Washington, Seattle, WA, 59 pp.
- Schmitt, R.W., J.M. Toole, R.L. Koehler, E.C. Mellinger and K.W. Doherty, 1988: The development of a fine- and microstructure profiler. *J. Ocean Atmos. Techno.*, **5**, 484-500.
- Schwiderski, E.W., 1981a: Global ocean tides. Part IV: The diurnal luni-solar declination tide (K_1). Atlas of tidal charts and maps. *Naval Surface Weapons Center*, Dahlgren, VA, TR81-142.

- Schwiderski, E.W., 1981b: Global ocean tides. Part V: The diurnal principal lunar tide (O_1). Atlas of tidal charts and maps. *Naval Surface Weapons Center*, Dahlgren, VA, TR81-142.
- Swaters, G.E., and L.A. Mysak, 1985: Topographically-induced baroclinic eddies near a coastline with application to the Northeast Pacific. *J. Phys. Oceanogr.*, **15**, 1470-1485.
- Thorpe, S.A., 1977: Turbulence and mixing in a Scottish loch. *Phil. Transac. Roy. Soc. London*, **286A**, 125-181.
- Thorpe, S.A., 1978: On the shape and breaking of finite amplitude internal gravity waves in a shear flow. *J. Fluid Mech.*, **85**, 7-32.
- Toole, J.M., K.L. Polzin and R.W. Schmitt, 1994: Estimates of diapycnal mixing in the abyssal ocean. *Science*, **264**, 1120-1123.
- Toole, J.M., R.W. Schmitt, K.L. Polzin and E. Kunze, 1996: Fine- and microstructure evidence of boundary mixing above the flanks of Fieberling Guyot. *J. Geophys. Res.*, submitted.
- Verron, J., and C. LeProvost, 1985: A numerical study of quasigeostrophic flow over isolated topography. *J. Fluid Mech.*, **154**, 231-252.
- Weller, R.A., 1982: The relation of near-inertial motions observed in the mixed-layer during the JASIN (1978) experiment to the local wind stress and to the quasigeostrophic flow field. *J. Phys. Oceanogr.*, **12**, 1122-1136.
- Wichman, C.A., C.C. Eriksen, N.M. Bogue, K.H. Brink, D.E. Frye, R.D. Pillsbury, G.M. Pittock and S.A. Tarbell, 1993: Fieberling Guyot moored array data. Tech. Rpt. A93-1, Oceanography, U of Washington, Seattle, WA, 373 pp.
- Wunsch, C., 1969: Progressive internal waves on slopes. *J. Fluid Mech.*, **35**, 131-144.
- Zhang, X., and D.L. Boyer, 1993: Laboratory study of rotating, stratified, oscillatory flow over a seamount. *J. Phys. Oceanogr.*, **23**, 1122-1141.
- Zyryanov, V.N., 1981: A contribution to the theory of Taylor columns in a stratified ocean. *Izvestiya, Atmos. Ocean Phys.*, **17**, 793-800.